CEMENT GEOCHEMISTRY OF PHOTOZOAN CARBONATE STRATA (UPPER CARBONIFEROUS–LOWER PERMIAN), FINNMARK CARBONATE PLATFORM, BARENTS SEA

S.N. EHRENBERG[1], N.A.H. PICKARD[2], T.A. SVÅNÅ[3], AND N.H. OXTOBY[4]

[1] Statoil, N-4035 Stavanger, Norway
e-mail: sne@statoil.com
[2] Cambridge Carbonates Ltd., Clematis Cottage, 41 Linthurst Newtown, Blackwell, Bromsgrove, Worcestershire, B60 1BP, U.K.
and Department of Earth Sciences, University of Wales, Cardiff CF1 3YE, U.K.
[3] Statoil, Postboks 40, N-9481 Harstad, Norway
[4] 41 Oaken Lane, Claygate, Esher, Surrey KT10 0RG, U.K. and Department of Geology, Royal Holloway, University of London, Egham, Surrey, TW20 0EX, U.K.

ABSTRACT: Stable-isotope, petrographic, microprobe, and fluid-inclusion analyses were carried out on calcite and dolomite cements from two cored wells covering the lower, high-porosity stratigraphic interval (Upper Carboniferous–Lower Permian) of the Finnmark carbonate platform. Cathodoluminescence petrography and microprobe profiling of cement zones reveal evidence for two main transitions in the cement growth history: (1) a possibly gradual and continuous transition from eogenetic (finely crystalline; < 0.1 mm) calcite and dolomite cements to mesogenetic (more coarsely crystalline) calcite and dolomite and (2) a discontinuous transition to a latest stage of saddle dolomite and anhydrite cementation. Fluid-inclusion data show that high-salinity brines replaced earlier marine to meteoric pore waters throughout the entire section prior to precipitation of the mesogenetic cements, possibly resulting from a series of brine-reflux episodes during successive stages of platform deposition. Carbonate $\delta^{13}C$ variations in both whole rocks and cements are related to proximity of shaly beds, from which isotopically negative organic carbon was released, probably during both eogenetic and mesogenetic diagenesis, to mix with isotopically positive marine-carbonate carbon. Carbonate cements show significant enrichment in Fe and Mn near shale, suggesting release during burial diagenesis of clay minerals. On the basis of the shallow-water setting of these strata during a time of major, high-frequency sea-level fluctuations, the absence of negative $\delta^{13}C$ excursions at cycle tops is suggested to reflect limited development of vegetation, possibly because of arid climate. The above results support the scenario of a photozoan platform succession undergoing extensive eogenetic stabilization with variable marine, evaporitic, and meteoric waters, followed by gradual mesogenetic cementation during progressive burial in a refluxed, hypersaline brine. This model contrasts with scenarios of extensive meteoric–phreatic calcite cementation indicated by cement-geochemistry studies of many other carbonate platforms, but it may be widely applicable to high-latitude Carboniferous–Permian sequences of similar depositional affinity.

INTRODUCTION

The geochemistry of cements in carbonate strata and their interpretation in terms of the evolution of pore fluids and porosity has been intensively studied during the past 15–20 years; however a number of fundamental controversies and uncertainties remain, including the relative importance of eogenetic versus mesogenetic cementation (terminology of Choquette and Pray 1970), the significance of cement geochemical zoning, the effects of subaerial exposure, and the prediction of reservoir quality (Schneidermann and Harris 1985; Moore 1989; Budd et al. 1995). Quantitative cement geochemical data are fundamental for evaluating models of carbonate diagenesis and are therefore also relevant to prediction of reservoir quality for the petroleum industry.

In this paper, we present an extensive stable-isotope dataset, supplemented by petrographic, microprobe, and fluid-inclusion analyses, characterizing the calcite and dolomite cements in a Carboniferous–Permian carbonate platform from the southern Barents Sea (Fig. 1; Ehrenberg et al. 1989a). Similarly comprehensive data on the diagenesis of late Paleozoic carbonates of the greater Barents Shelf area have not been available previously. These strata are currently of interest to the petroleum industry because they constitute an important potential petroleum province in their own right (Stemmerik et al. 1999) and are also potential analogs for major petroliferous carbonate platforms in the former Soviet Union, including both the Timan–Pechora province of northern Russia (Martirosyan et al. 1998) and the Pricaspian basin of Kazakhstan (Nevolin and Fedorov 1995).

Our results constrain depositional and burial conditions during cementation and provide a basis for future work evaluating the processes controlling the wide porosity variations in these rocks (Fig. 2). Porosity and permeability controls are not treated in this paper, but an overview of the problems involved was given by Ehrenberg et al. (1998b). The data are organized in four sections:

1. Profiles of whole-rock stable-isotope analyses through the cored intervals are presented to define the framework for interpreting the cement data.

2. Representative examples are shown of cement petrography and chemical composition at various stratigraphic levels.

3. Fluid-inclusion analyses constrain temperatures of cementation, the salinity of the waters involved, and whether petroleum was present during cement growth.

4. Stable-isotope analyses of different cement generations are examined.

These results are then interpreted in terms of a model for the major processes controlling cement chemistry and petrography. Finally, the data are compared with earlier stable-isotope datasets from other Barents Shelf carbonate sections, providing an indication of the variability within this large and relatively little-known province.

BACKGROUND

Depositional Setting

Well 7128/6–1 is regarded as the "stratigraphic reference section" for the entirely subsurface Finnmark carbonate platform (Fig. 1) because of its extensive core coverage (445 m of the 527 m Upper Carboniferous through Upper Permian section) and the relatively complete stratigraphy preserved at this location. The sedimentology, biostratigraphy, sequence stratigraphy, and diagenesis of this succession are described by Bugge et al. (1995), Ehrenberg et al. (1998a, 1998b), Ehrenberg et al. (2000a), and Ehrenberg et al. (2000b).

The strata are divisible into nine lithostratigraphic units (L-1 to L-9), which are interpreted as comprising seven main depositional sequences (S-1 to S-7). The lower part of this succession (units L-1 through L-7; late Moscovian–early Sakmarian) was deposited under warm-water, "photozoan" (James 1997) conditions, whereas the upper part (units L-8 and L-9; late Sakmarian through Late Permian) was deposited under cool-water "heterozoan" conditions. Except for occurrences of porous spiculitic chert at the top of unit L-9, the heterozoan strata have low porosity due to a combination of shaly composition and extensive burial cementation (Ehrenberg et al. 1998b).
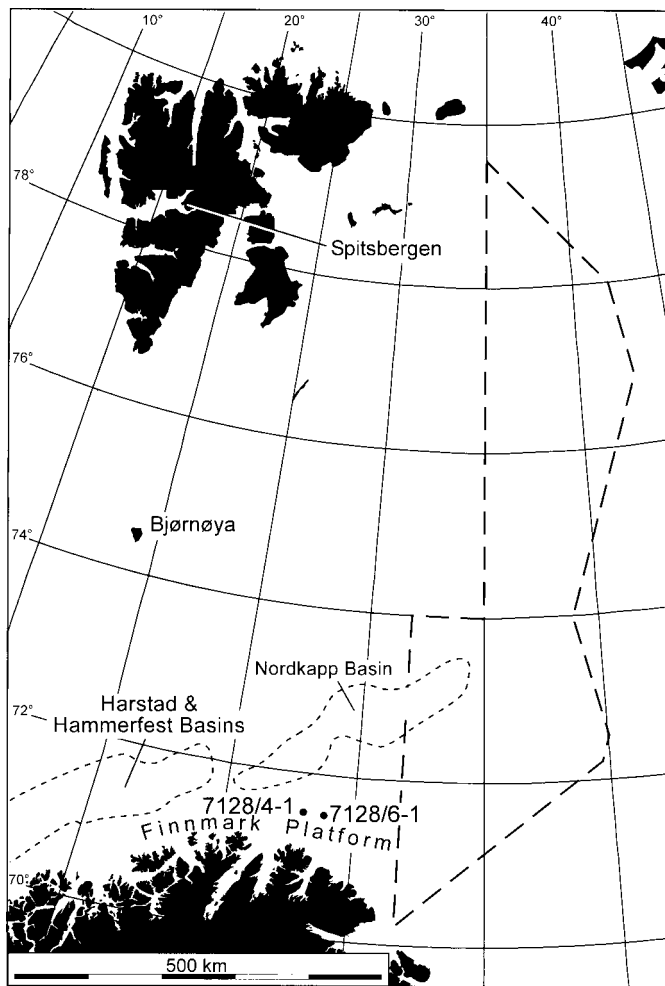
FIG. 1.—Map showing location of wells studied. The ''Finnmark carbonate platform'' (stratigraphic entity) is roughly equivalent in area with the ''Finnmark Platform'' (structural entity; labeled on map), except that carbonate strata pass laterally into a siliciclastic-dominated section in the western part of the Finnmark Platform. The Upper Paleozoic carbonate platform strata are 527 m thick in well 7128/6–1; thin to roughly half that value adjacent to the line of their erosional truncation near the Norwegian mainland; and thicken to 1100–1300 m adjacent to the Nordkapp basin. The same platform strata are believed to continue eastward through the disputed boundary zone with Russia (long dashes) and thence southeastward along the Kola Monocline. The fault-bounded Nordkapp Basin contains thick salt deposits believed to have formed during relative sea-level lowstands when the Finnmark carbonate platform was subaerially exposed. Age-equivalent, lithologically similar carbonate units crop out on the islands of Spitsbergen and Bjørnøya (Ehrenberg 1998a). The pointer line indicates the area of Spitsbergen sampled for the dataset in Figure 18A.

FIG. 2.—Lithology, sequences, and porosity profile in cored portions of units L-1 through L-7 of wells 7128/4–1 and 7128/6–1. Lithology is indicated by color and lithology column width: BLACK = shale (Sh); YELLOW = siltstone (Si) and sandstone (Ss); RED = dolomitic mudstone (M); BLUE = wackestone (W), packstone (P), and grainstone (G); GREEN = phylloid algae and/or *Palaeoaplysina* buildup (B). Inferred surfaces of extended subaerial exposure are indicated by short red lines to right of lithology log. Depths of buildup samples analyzed by microprobe profiles of cement chemistry (Figs. 6, 7, 8, and 9) are shown by black arrows to right of lithology log. Age constraints from fusulinid dating (Ehrenberg 2000a) are shown as arrow brackets. Tops of major depositional sequences (RED lines) are labeled S-1, S-2, etc. Tops of lithostratigraphic units (BLACK lines) are labeled L-1, L-2, etc. Maximum-flooding surfaces (base-level rise/fall turnaround) are shown as BLUE dashed lines. Porosity profile shows core plug measurements within cored intervals and wireline-log porosity outside of core coverage.

The present paper is concerned only with the lower, photozoan part of the succession (units L-1 through L-7), consisting in well 7128/6–1 of 316 m of cyclic carbonates and subordinate siliciclastics (Fig. 2). This interval contains numerous high-porosity intervals and is regarded as highly prospective with regard to reservoir quality throughout the Barents Sea province (Stemmerik et al. 1999). The upper part of this interval (units L-6 and L-7) was also cored 26 km due west of well 7128/6–1 in well 7128/4–1 (Fig. 1), providing information about lateral sedimentologic and diagenetic variability along depositional strike.

The Late Carboniferous–Early Permian paleogeography of the Finnmark carbonate platform consisted of a broad shallow shelf that shoaled landward toward the present Norwegian mainland and deepened northward toward various poorly defined shelf-margin locations somewhere between the stud-
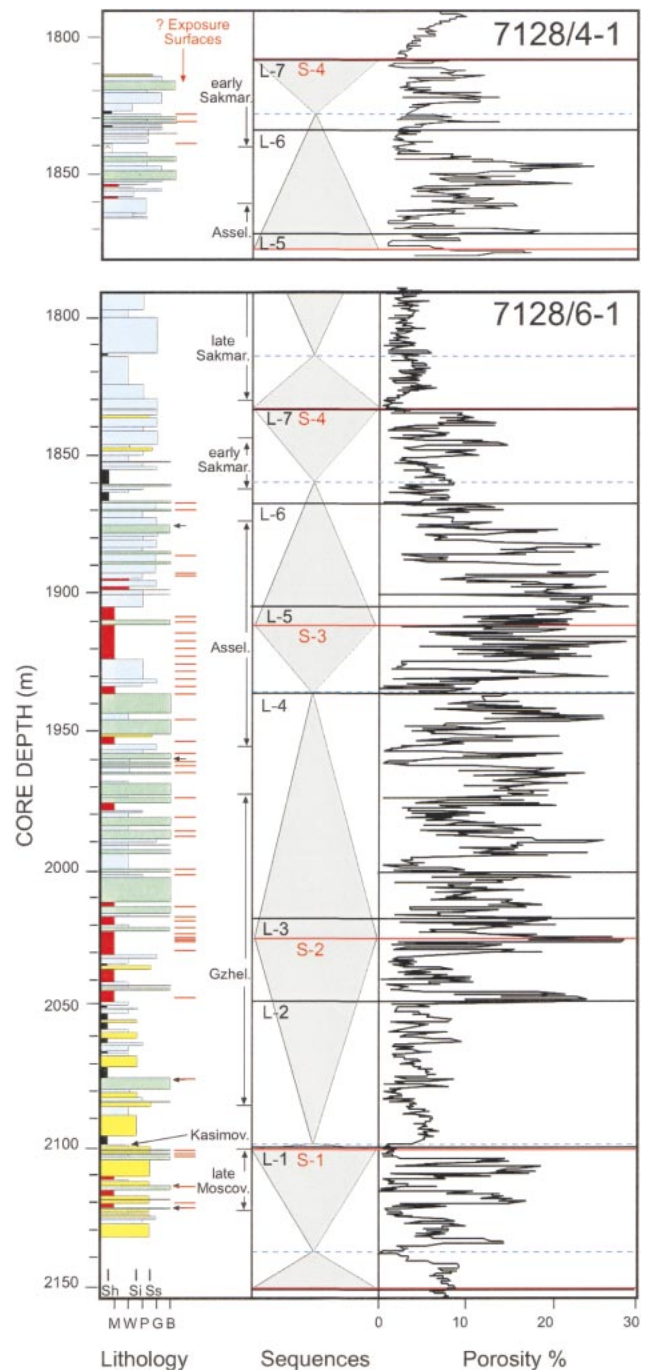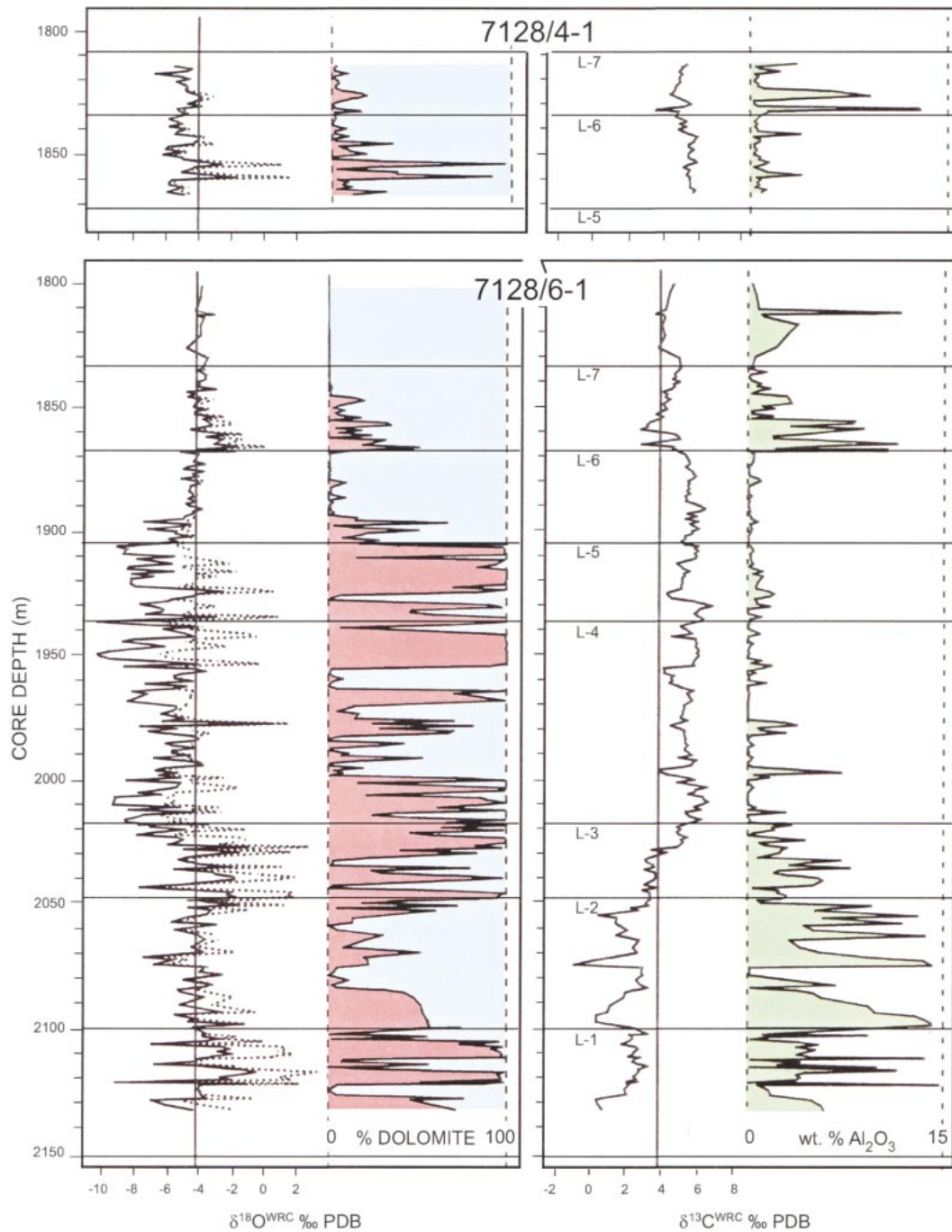
Fig. 3.—Profiles of whole-rock-carbonate oxygen and carbon isotope compositions from cored intervals in wells 7128/4–1 and 7128/6–1. Solid vertical reference lines are drawn at $-4‰$ $\delta^{18}O$ and $+4‰$ $\delta^{13}C$. Measured $\delta^{18}O^{WRC}$ values (dotted curve) have been corrected for dolomite content to $\delta^{18}O^{WRC}_C =$ equivalent pure-calcite values (solid curve) using Equation 1. Separation between these curves is proportional to dolomite content. Dolomite % in total carbonate fraction (from bulk XRD or petrographic estimation) is shown to right of $\delta^{18}O$ track, with dashed reference lines at 0 and 100%. Weight % Al_2O_3 is shown to right of $\delta^{13}C^{WRC}$ track, with dashed reference lines at 0 and 15%. Alumina is an index of siliciclastic content (correlates strongly with gamma-ray activity).

ied well locations and the Nordkapp basin (Fig. 1), where thick evaporite units were deposited during Late Carboniferous–Early Permian lowstands of relative sea level. Paleogeographic maps by Golonka and Ford (2000) show the paleolatitude of the southernmost Barents Sea area to have been roughly 28° N in Late Carboniferous time, increasing to 30° N in the Early Permian.

The burial history of the strata is divisible into three stages: (1) gradual accumulation of the 500-m-thick Upper Carboniferous through Permian platform section; (2) more rapid burial under a thick Triassic and relatively thin Jurassic–Lower Tertiary section, estimated as having been roughly 2–2.5 km thick in the well locations; and (3) uplift and erosion of roughly 1–1.5 km of section mainly at 40–30 Ma, but continuing at 10–5 Ma, according to an unpublished apatite-fission-track study reported in 1998 by Geotrack International Pty. Ltd. A drill-stem test in unit L-9 of well 7128/4–1 indicated 49°C at 1.18 km below sea floor and an estimated geothermal gradient of 38.8°C/km, giving a present temperature range of 75–60°C from

the base of unit L-1 to the top of L-7. The vitrinite reflectance trend for this interval is in the range 0.6–0.7% Rm (Ehrenberg et al. 1998b). The fluid-pressure gradient is only slightly above hydrostatic.

Lithology and Sequence Stratigraphy

Lithostratigraphic units L-1 through L-7, each corresponding to a distinctive lithologic association, are interpreted as making up depositional sequences S-1 through S-4, each corresponding to a large-scale transgressive–regressive cycle of facies succession and each containing numerous component cycles. Cycle bases are typically defined by a sharp transition to deeper-water facies, commonly associated with higher clay content, followed by gradual shoaling upward to the cycle top. Dating of these strata is based on fusulinid biostratigraphy (Ehrenberg et al. 2000a). More recently, the technique of graphic correlation (Groves and Brenckle 1997) has been applied to these data by V.I. Davydov (personal communication) to greatly increase the resolution with which the durations of the component depositional sequences can be measured.

Sequence S-1.—The uncored lower part of this sequence consists of a quartz-pebble conglomerate overlain by a transgressive shale. The cored upper part (unit L-1; late Moscovian) consists of three main cycles of dolomitic sandstone overlain by thin limestone beds, including phylloid algae buildup beds, 0.2–2 m thick. The top of S-1 is a hiatus of roughly 0.5 My duration. At this point there is a major change from shallow-water, sandstone-dominated lithofacies to deeper-water, shale-dominated lithofacies.

Sequence S-2.—Unit L-2 consists of seven cycles of shale overlain by calcareous siltstone to silty wackestone. The lowermost of these cycles is the thickest (25 m) and is capped by 4 m of phylloid algae–*Palaeoaplysina* buildup. Unit L-3 consists mainly of thin-bedded dolomitic mudstone–siltstone with anhydrite nodules, interpreted as representing a shallow hypersaline lagoonal setting. This transition from thicker shale/limestone cycles (L-2) to thin dolomitic mudstone cycles (L-3) is a long-term shoaling trend, interpreted as sequence S-2 (Kasimovian through late Gzhelian; 6 My duration). Sequences S-1 and S-2 have widely varying, generally high siliciclastic content and gamma ray (GR) activity, reflecting waning tectonism and gradual erosion/burial of structural highs following mid-Carboniferous rifting.

Sequence S-3.—At the top of S-2, siliciclastic influx decreased markedly, corresponding to the beginning of a long-term transgressive trend expressed by an 80 m-thick section composed mainly of *Palaeoaplysina* buildups and fusulinid wackestones (unit L-4). This unit displays two scales of internal cyclicity: (1) a larger, cyclothem-scale cyclicity, expressed by uranium-rich GR peaks overlain by thicker (12–19 m thick) low-GR intervals, and (2) a finer-scale cyclicity, consisting of wackestone–buildup cycles (1–7 m thick) contained within the low-GR, highstand intervals of the larger-scale cycles (Fig. 2). The overlying unit L-5 consists of 10 m of coated-grain packstone–grainstone followed by 19 m of thin-bedded dolomitic mudstone. This progression from aggradational wackestone–buildup cycles (L-4) to grain shoals (lower L-5) to thin, restricted lagoonal–sabkha cycles (upper L-5) is a long-term shoaling trend, interpreted as sequence S-3 (late Gzhelian through mid-Asselian; 5 My duration).

Sequence S-4.—The S-3 sequence boundary corresponds with the overall turning point in lithofacies development throughout the Upper Carboniferous–Lower Permian platform succession, from upward-decreasing to upward-increasing accommodation, and is therefore identified as a second-order sequence boundary. A neodymium-isotope profile of the 7128/6–1 section shows that this horizon corresponds to a major change in siliciclastic provenance signature, interpreted as reflecting a renewal of basement erosion and possibly indicating a tectonic component of hinterland uplift at this point (Ehrenberg et al. 2000b). Unit L-6 is a stack of poorly defined packstone–grainstone cycles 41 m thick, the lower part of which contains the maximum porosity development in the upper Paleozoic section (Fig.

2). The upward-decreasing porosity trend of unit L-6 reflects a subtly retrogradational depositional pattern, with abrupt maximum flooding occurring as a series of two calcareous shale beds at the base of unit L-7 (Fig. 2). The overlying section shows a pronounced shoaling trend, with thin beds of calcareous sandstone appearing in the upper part of unit L-7. Units L-6 and L-7 thus display a long-term transgressive–regressive pattern, interpreted as comprising sequence S-4 (mid-Asselian through early Sakmarian; 6 My duration). The top of S-4 represents the termination of shallow–warm-water depositional conditions on the Finnmark platform and apparently also throughout the Barents Sea. The overlying unit L-8, equivalent to sequence S-5 (late Sakmarian through Artinskian; 11 My duration), consists of tightly cemented bryozoan–echinoderm–brachiopod grainstones–packstones having only minor photosynthesis-dependent components (fusulinids and red algae).

Subaerial Exposure Surfaces

Insofar as the Late Carboniferous to Early Permian was a time of high-amplitude, high-frequency sea-level fluctuations (Veevers and Powell 1987; Ross and Ross 1988; Heckel 1994), numerous subaerial exposure surfaces are expected in shallow-water carbonate successions of this age worldwide. In the case of the Finnmark carbonate platform, this expectation is supported by well-developed exposure surfaces in time-equivalent and lithologically similar strata outcropping on the islands of Spitsbergen and Bjørnøya (Fig. 1; Pickard et al. 1996; Stemmerik and Larssen 1993).

These outcrop studies demonstrate that exposure surfaces typically have great lateral variation in degree of development, such that unambiguous recognition of exposure in one-dimensional core studies is likely to be problematic. *Microcodium* (Klappa 1978) is a common indicator of exposure in the Spitsbergen strata, but it has been found in only one place in the present cores: in limestone lenses having stylolitic contacts within a 2-cm-thick shale layer at 1886.95 mCD (core depth) in well 7128/6–1. At numerous other depths, the presence of exposure surfaces has been inferred on the basis of suggestive but not compelling evidence, including: (1) bleaching, truncation of laminations and bioclasts, or brecciation and rip-up clasts at a sharp discontinuity corresponding to a cycle top, where a deeper-water facies overlies shallower-water deposits; (2) infilling of apparent dissolution cavities in the underlying layer by overlying sediment; and (3) a layer of small anhydrite nodules sharply overlain by shale laminae. Nowhere is the interpretation of exposure unambiguous, and many of these surfaces could alternatively be explained as the product of submarine exposure (Shinn 1986). Evidence for pervasive meteoric diagenesis is provided by abundant molds of originally aragonitic bioclasts throughout units L-1 to L-7 (Ehrenberg et al. 1998b).

ANALYTICAL METHODS

Whole-rock oxygen and carbon isotope analyses were performed using finely ground material previously analyzed for bulk chemical composition (Ehrenberg et al. 1998a). Samples have uniform one-meter spacing in units L-1 through L-7 and two-meter spacing in L-8 and L-9. Samples (50–100 mg) were digested for 15 minutes in concentrated phosphoric acid at 80°C to release CO_2, which was then analyzed using a Finnigan 251 gas-source mass spectrometer. Comparisons of isotopic values of splits of the sample material digested in concentrated phosphoric acid at 80°C showed no systematic differences between splits digested for 18 versus 32 minutes. Data are reported in per mil versus Vienna Pee Dee Belemnite (‰ PDB). A laboratory standard shows reproducibility of 0.05‰ for $\delta^{13}C$ and 0.09‰ for $\delta^{18}O$. As a standard procedure, samples are rerun if the ''SA44'' value (amplified voltage of the signal recorded in the mass spectrometer cups) is under 3 V (higher voltages give better signal/noise ratios). Microsampling for stable-isotope analysis of cements was performed by scraping material

from polished thin sections using a binocular microscope and cathodolu-minescence maps of the sampled areas.

Microprobe analyses were performed using a JEOL JXA 8600 Super-probe operated through Oxford Instruments AN10000 with LEMAS auto-mation control. Conditions were 15 kV accelerating potential; 10 nA beam current on faraday cup; 30 seconds counting time on peaks (15 s for Ca); 5–10 micron beam raster. Standards were acquired under the same beam conditions (magnesite for Mg; albite for Na; calcite for Ca; hematite for Fe; MnO for Mn; barite for S; $SrTiO_6$ for Sr; diopside for Si).

Fluid-inclusion analyses were performed using a Nikon epi-fluorescence microscope for identification of petroleum inclusions, and a Linkam TMS90/THM600 heating–cooling stage calibrated with international stan-dards for microthermometry. Precision of phase-change temperatures using temperature cycling is $\pm$ 0.1°C, and accuracy is better than 1°C throughout the temperature range. Final ice melting temperatures are converted to sa-linities using the transform of Oakes et al. (1990) for the system NaCl–$CaCl_2$–H_2O, giving an accuracy of ca. $\pm$ 1000 ppm (0.1 wt. %). Measure-ments were performed on doubly polished rock wafers around 100 microns in thickness, fabricated at low temperature. After inclusions were identified and mapped, homogenization temperatures were measured in order of in-creasing temperature, followed by freezing experiments. Final ice melting data for monophase inclusions were obtained by artificially stretching to nucleate a vapor bubble.

DATA

Whole-Rock-Carbonate Stable-Isotope Profiles

Profiles of whole-rock carbonate oxygen ($\delta^{18}O^{WRC}$) and carbon ($\delta^{13}C^{WRC}$) isotope compositions were measured (Fig. 3) to aid in inter-preting depositional and diagenetic history and for possible use in inter-well stratigraphic correlation. High-resolution whole-rock oxygen and car-bon isotope profiling of carbonate strata is a well established technique applicable to both of these uses (Wagner et al. 1995; Saller et al. 1999; Immenhauser et al. 2000). Comparison of isotope profiles between wells 7128/6–1 and 7128/4–1 is possible in units L-6 and L-7, which were cored in both wells (Fig. 4).

The $\delta^{18}O^{WRC}$ profile is strongly affected by variations in calcite/dolomite ratio because measured $\delta^{18}O$ is systematically higher by approximately 3.8‰ for dolomite relative to calcite equilibrated under identical conditions of temperature and water composition (Land 1983). Thus, the $\delta^{18}O^{WRC}$ values plotted in Figures 3 and 4 have been corrected to equivalent pure-calcite values by the following formula:

$$\delta^{18}O_C^{WRC} = \delta^{18}O_{MEASURED}^{WRC} - 3.8(DOL/(DOL + CAL)) \quad (1)$$

where DOL and CAL are the weight % dolomite and calcite determined by bulk X-ray diffraction or, in a subordinate number of cases (11 of 314 total), by qualitative petrographic estimation. This correction does not im-ply or require that the dolomite component of each sample was ever in isotopic equilibrium with calcite; it merely recasts the bulk isotope value as equivalent calcite for the purpose of developing a consistent profile for stratigraphic comparison.

Regarding the $\delta^{13}C^{WRC}$ profile, a most interesting feature is its strong negative correlation with siliciclastic content, as represented by whole-rock alumina (Figs. 3, 5), a general index of siliciclastic (aluminosilicate) con-tent, which is strongly negatively correlated to bulk carbonate content and strongly positively correlated to spectral K and Th gamma-ray activity (Eh-renberg and Svånå 2001). Thus, in the carbonate-dominated units L-4 through L-8, $\delta^{13}C^{WRC}$ is mainly in the range +4 to +6‰ PDB, whereas in the siliciclastic-rich units L-1 to L-3, $\delta^{13}C^{WRC}$ is mostly lower than +3.5.

Cement Petrography and Chemical Composition

This section presents petrographic descriptions and electron microprobe analyses of representative examples of carbonate cement types from dif-ferent stratigraphic levels in well 7128/6–1. The examples were selected from phylloid algae–*Palaeoaplysina* buildup facies, characterized by a fab-ric of fragmented plates enclosed in widely varying proportions of micro-peloidal mud matrix. Cements in these buildups have petrographic appear-ance similar to cements in surrounding non-buildup lithologies, except that larger areas of coarse cement are present, filling molds after aragonitic plate fragments or cavities within whole brachiopod shells. Locations of the sam-ples studied are shown by arrows in Figure 2.

The descriptive cement terminology used in this study (Table 1) is based on crystal size and morphology, as observed using a conventional light microscope. Cementation of L-1 through L-7 carbonates is interpreted to have occurred in the diagenetic sequence described in Table 2. Diagenetic stages 2, 3, and 4 (eogenetic conditions) probably were broadly overlapping and variable in relative timing in different parts of the stratigraphic section. Stages 5, 6, and 7 represent continued cement growth with gradually in-creasing temperature and burial depth. Stage 8 cements truncate earlier generations and thus represent a distinctly later episode.

Calcite.—The calcite cements analyzed are broadly categorized as either ''early'' fine spar (< 0.1 mm) or ''late'' coarse spar (0.1–1 mm). Fine spar lines bioclasts and early secondary dissolution molds and is overgrown by the coarse spar. Both fine and coarse spar are volumetrically abundant (commonly 10–20%), but proportions vary greatly from sample to sample. The volumetrically minor fibrous and syntaxial varieties listed in Table 1 have not been analyzed in this study, but stable-isotope data for volumet-rically major syntaxial calcite cement in unit L-8 are reported by Ehrenberg et al. (1998b).

The stratigraphically deepest cements analyzed are from buildup beds at 2114.75 and 2122.00 m in unit L-1 and 2076.00 m in unit L-2 (Fig. 3). Figure 6 shows the cement sequence infilling a brachiopod shell from 2122.00 m. This sequence begins with a lining of fine prismatic (''dog-tooth'') spar having mottled nonluminescent to bright CL, moderate to high Mg, and low Fe. The overlying coarse spar has pronounced CL zoning consisting of: (1) a moderate-CL zone having low Mg and Fe; (2) a bright-CL zone with moderate Fe and high Mn; (3) a thin nonluminescent zone with moderate Mg and high Fe; and (4) an outer dull-CL zone with variable Mg and moderately high Fe. Average compositions of each cement zone are listed in Table 3. Two other examples (2114.75 and 2076.00 m; not illustrated here) show similar compositional and CL zoning infilling phyl-loid algae molds and brachiopod shells.

In contrast to the L-1 and L-2 examples, the coarse calcite cements at higher stratigraphic levels (L-4 to L-7) mostly show only minor Fe and Mn enrichment, as observed both with microprobe analyses and by staining of thin sections. Exceptions are thin limestone beds interlayered with shales at the base of unit L-7 and calcareous sandstones in upper L-7, where prominent Fe-zoning is revealed by staining.

A typical example from an undolomitized, tightly calcite-cemented buildup at 1960.00 m in unit L-4 is illustrated in Figure 7. The cement sequence begins with a thin coating of Mg-rich fine mosaic spar lining the walls of the *Palaeoaplysina* mold. The overlying coarse spar zoning sequence consists of: (1) dull-CL, finely concentrically zoned, coarse spar crystals growing from the walls; (2) a thin bright-CL zone having slightly higher Mn than the previous dull-CL zone; and (3) the final, volumetrically dominant zone of faintly zoned, moderate-CL spar with moderate Mg and very low but subtly outward-increasing Fe and Mn. Average compositions of each cement zone are listed in Table 3. The earliest coarse spar Zone 1 contains regions of very low Mg content similar to the low-Mg part of Zone 1 in the 1877.25 example described below.

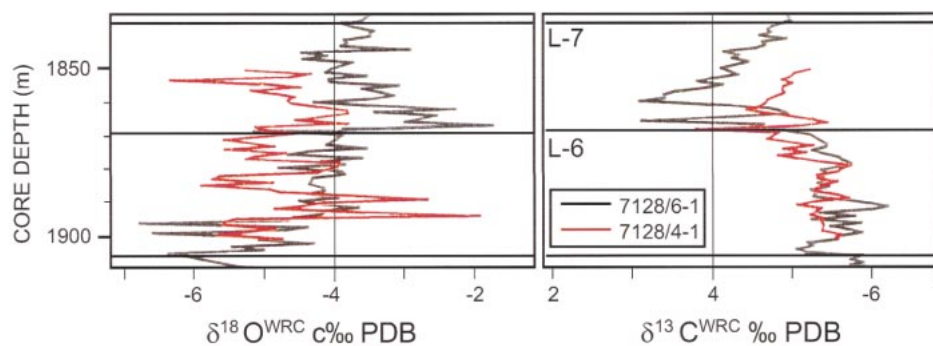The shallowest example is from a buildup at 1877.25 m in unit L-6 (Fig.

Fig. 4.—Comparison of $\delta^{18}O^{WRC}_C$ and $\delta^{13}C^{WRC}$ profiles in units L-6 and L-7 of wells 7128/4–1 and 7128/6–1. Tops of lithostratigraphic units in 7128/6–1 (horizontal lines) are labeled in the $\delta^{13}C^{WRC}$ track. The depth scale refers to well 7128/6–1. Curves for well 7128/4–1 have been shifted downward 35.1 m to match the depth of the L-6/L-7 boundary in 7128/6–1.

8). Here the coarse spar shows a zoning sequence consisting of: (1) an innermost zone of nonluminescent to dull-CL cement with very low to moderate Mg content; (2) a bright-CL zone of slightly higher Mn and near-zero Fe; and (3) an outer dull-CL zone of low Mn and subtly increasing Fe. Key components from the three representative examples in Figures 6–8 are plotted for comparison in Figure 9.

Fine calcite cement was also analyzed from two partly dolomitized, porous buildups in unit L-4 (1976.00 and 1972.00 m) and from two forami-nifera-rich grainstone–packstones in unit L-6 (1902.00 and 1891.75 m). These crystals have low Fe and Mn, moderate to high Mg, and widely variable Na, S, and Sr (Table 3).

Dolomite.—The dolomite cements analyzed are broadly categorized as fine dolomite (< 0.1 mm; Fig. 10); coarse spar (0.1–1 mm; Fig. 11); and saddle dolomite (Table 1). Abundances and relative proportions of each vary greatly from sample to sample. Saddle dolomite is especially abundant in limestone beds of units L-1 and L-2 and is absent to minor in overlying units. Coarse dolomite is present in minor amounts ($< 3\%$) or absent,

except in extensively dolomitized buildup and grain-dominated lithologies, where it is commonly a major constituent.

The term ''fine dolomite'' includes both xenotopic-cloudy matrix-repla-cive dolomite and euhedral-limpid cement crystals. In extensively dolo-mitized mudstones and wackestones, these two end-member varieties of fine dolomite commonly occur intimately associated in sediments originally occupied by carbonate mud (Fig. 10C–F). In little-dolomitized packstones, grainstones, and sandstones, fine dolomite is localized in intergranular areas of former carbonate mud, now represented by very fine, equant calcite (Fig. 10A, B). The fine dolomite has moderate red-orange CL (Fig. 11).

Microprobe analyses of fine dolomite were obtained from six samples, including four samples of completely dolomitized mudstone in units L-5 and L-3 and two moderately dolomitized grainstones in unit L-6 (Fig. 12A, B). These crystals show wide variations in Fe, Mn, Na, Sr, and S (Fig. 12A, B; Table 3). Fine dolomite was also analyzed from three buildups in unit L-4 (2009.85, 1976.00, and 1972.00 m; Fig. 12C, D). These analyses are mostly low in Fe, Mn, Sr, Na, and S, but exceptions include the Fe-enriched rims of some fine dolomite crystals (Table 3) and a few analyses with high Na and S (Fig. 12D).

''Coarse dolomite'' consists of clear euhedral rhombs that either fill pore spaces or replace calcite matrix and bioclasts. CL petrography reveals that coarse dolomite crystals have commonly formed as overgrowths on more strongly luminescent fine dolomite rhombs (Fig. 11). However, only a mi-nor proportion of the more abundant fine rhombs are overgrown to coarser size. Coarse dolomite mostly has very dull CL, reflecting Fe-rich compo-sition, but one thin zone of bright-CL is commonly present, corresponding with a sharp drop in Fe content (Fig. 11). Coarse dolomites were analyzed from three partly to completely dolomitized, porous buildups in unit L-4
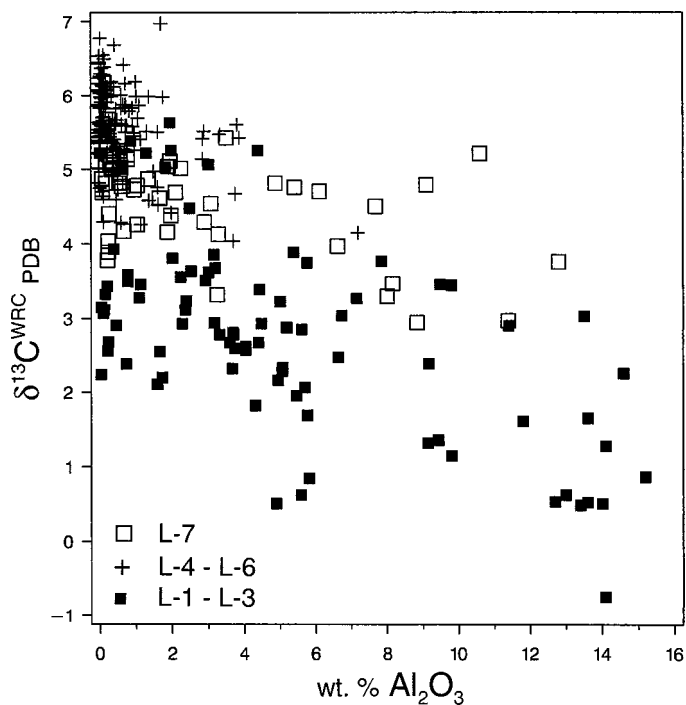

Fig. 5.—Whole-rock-carbonate carbon isotope composition versus bulk alumina content in units L-1 through L-7 of wells 7128/4–1 and 7128/6–1. Overall decreasing $\delta^{13}C^{WRC}$ values with increasing alumina is suggested to reflect local contribution of isotopically negative carbon from organic matter associated with argillaceous deposits. Plotting symbol indicates lithostratigraphic unit.

TABLE 1.—*Terminology for carbonate cement morphologies observed in thin section.*

CALCITE:	
Fibrous*	Crust of radial fibrous cement (<0.5 mm thick)
Micropeloidal*	Clear crystals (0.01–0.02 mm) surrounding micritic peloids (generally 0.01–0.03 mm in diameter).
Fine*	<0.1 mm. Subvarieties include microspar (<0.02 mm) and fine-equant spar, typically replacing mud matrix, and prismatic (''dog-tooth'') spar, lining bio-clast walls.
Coarse	0.1–1 mm. Equant crystals infilling former pore spaces.
Syntaxial	Overgrowths on echinoderm fragments (<0.3 thick).
Microcodium	This distinctive cement type (Klappa 1978) is observed in only one place; with-in stylolitically thinned limestone lenses in a 2-cm-thick shale layer at 1886.30 m in well 7128/6–1.
DOLOMITE:	
Fine*	<0.1 mm. Subvarieties include microdolomite (<0.02 mm) and xenotopic to euhedral fine dolomite. Cloudy (inclusion-rich) core areas are typically over-grown by clear (inclusion–poor) rims. Fine dolomite occurs both as a re-placement of matrix and bioclasts and as cement, typically filling micropores in matrix areas.
Coarse	0.1–1 mm. Pore-filling euhedral rhombs.
Saddle	Pore-filling crystals (0.1–2 mm) with sweeping extinction and curved surfaces.

* These relatively early, finer-grained cements typically have bright to moderate blue-light fluorescence (Dravis and Yurewicz 1985). Coarser cements are nonfluorescent.
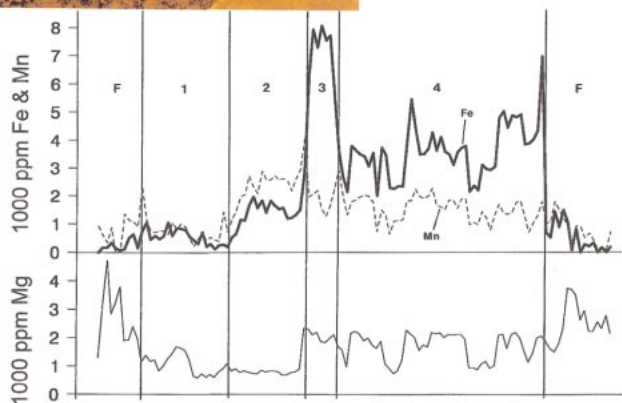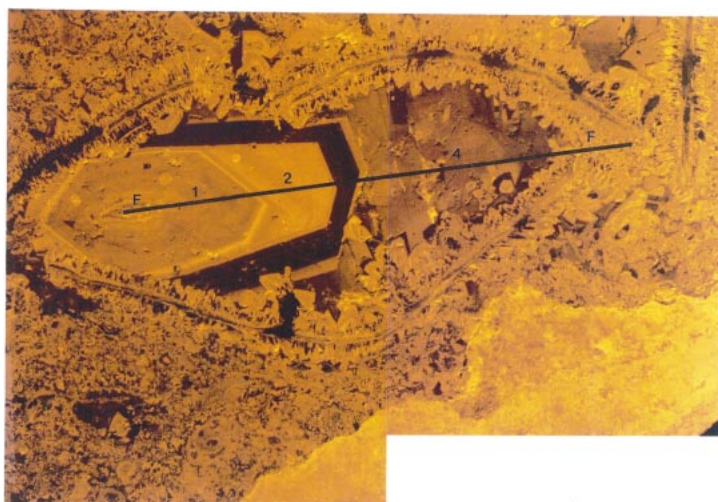
Fig. 6.—Cathodoluminescence photo showing calcite cements infilling the interior of a brachiopod shell in a phylloid algae buildup at 2122.00 m core depth in well 7128/6–1 (unit L-1). Line shows path of microprobe traverse. Note that the early fine spar (prismatic ''dog-tooth'' lining on brachiopod) consists of an inner non-CL zone overlain by an outer zone with bright–dull CL zoning. Profiles of Fe, Mn, and Mg are plotted below at the same horizontal scale as the traverse line in the photo, with cement zones labeled as on photo: F = early generation of fine prismatic spar; 1 = coarse spar zone 1; 2 = coarse spar zone 2; 3 = coarse spar zone 3; 4 = coarse spar zone 4. Zones 1–3 are part of a single crystal, but zone 4 is composed of several smaller crystals, which are interpreted as being roughly equivalent to the thin outermost zone of the coarse crystal with zones 1–3.
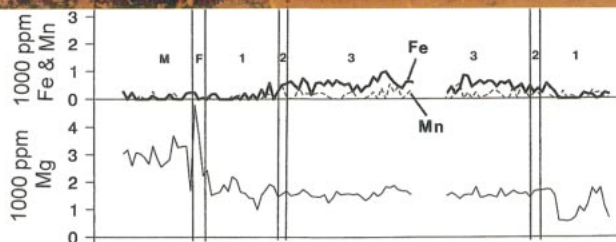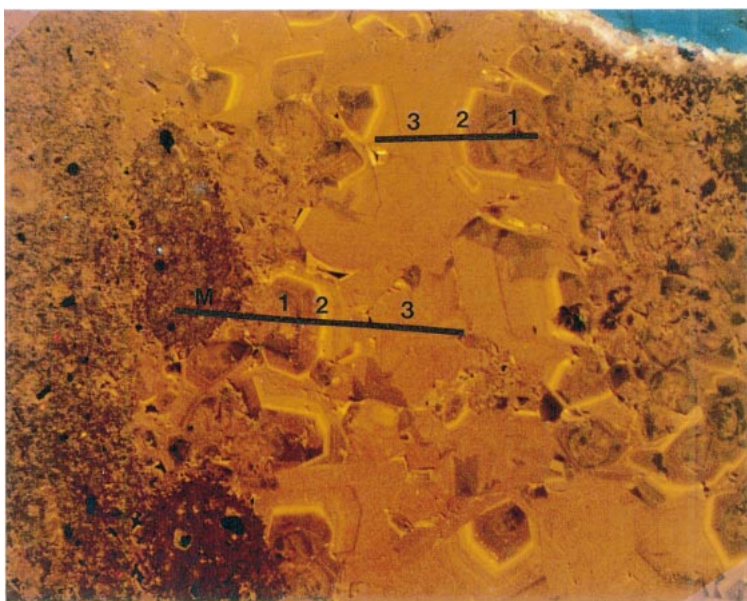

Fig. 7.—Cathodoluminescence photo showing calcite cements infilling the interior of a *Palaeoaplysina* mold in a buildup at 1960.00 m core depth in well 7128/6–1 (unit L-4). Lines show paths of two microprobe traverses. Profiles of Fe, Mn, and Mg are plotted below at the same horizontal scale as the traverse line in the photo (lower traverse at left), with cement zones labeled as on photo: M = mud matrix filling a *Palaeoaplysina* canal; F = early generation of fine prismatic spar; 1 = coarse spar zone 1; 2 = coarse spar zone 2; 3 = coarse spar zone 3. In each traverse, zones 1 and 2 and the first part of zone 3 are from a single crystal, but the last part of zone 3 extends into adjacent crystals. Note that zone 1 in the second (upper) traverse includes an early zone of very low-Mg composition.

TABLE 2.—*Sequence of main diagenetic processes affecting carbonate strata throughout units L–1 through L–7 of the Finnmark carbonate platform (slightly modified from Ehrenberg et al. 1998b).*

===
============= EOGENETIC DIAGENESIS =============

1. *Marine cementation*—represented by rare fibrous calcite and micropeloidal calcite cement (abundant in buildup facies).
2. *Aragonite dissolution*—ascribed to subaerial exposure and leaching by meteoric water.
3. *Early calcite cementation*—fine spar lining bioclasts and molds; probably formed as shallow phreatic cements from both marine and meteoric waters.
4. *Early dolomitization and anhydrite–gypsum cementation*—fine dolomite, including both mud–replacive (cloudy, inclusion–rich) and fine cement (clear, inclusion–poor) varieties. Minor, local barite and celestite cements are commonly associated with anhydrite–gypsum.

============= MESOGENETIC DIAGENESIS =============

5. *Quartz cementation*—overgrowths on quartz grains and occasional small volumes of silicified carbonate rock.
6. *Burial dolomite cementation*—coarse dolomite with concentric dull to bright CL zoning. Some fine dolomite may also have formed during burial.
7. *Burial calcite cementation*—coarse spar with concentric dull to bright CL zoning. Much of the fine calcite spar has similar CL characteristics, and may therefore represent the earlier stages of burial cementation. Most syntaxial calcite cement (overgrowths on echinoderm fragments) is also interpreted to have formed during burial.

============= LATEST MESOGENETIC DIAGENESIS =============

8. *Saddle dolomite and coarse anhydrite cementation.*
===

(2009.85, 1976.00, and 1972.00 m). These analyses have widely variable Fe and Mn, the pattern of which is partly revealed by backscattered-electron images showing concentric zoning and overall patterns of outward Fe-enrichment (Figs. 11, 12). Na, Sr, and S are generally low (Table 3).

''Saddle dolomite'' (Spötl and Pitman 1998) varies from anhedral, where pore space has been completely filled, to euhedral, where crystals are surrounded by open pore space. CL is mainly absent to very dull, but a few samples with moderate-dull CL zoning have been observed (Ehrenberg et al. 1998b). Saddle dolomite is commonly associated with coarse anhydrite cement, and both phases commonly truncate zoning in coarse calcite spar. A series of six microprobe analyses was obtained from saddle dolomite in a buildup in unit L-2 (2077.00 m), and one analysis was obtained of saddle dolomite in L-4 (1976.00 m). The L-2 analyses straddle the compositional boundary between dolomite and ankerite, whereas the L-4 analysis is similar to the more Fe-rich coarse dolomite in the same sample, except that Mn is below detection (Table 3).

Fluid Inclusions

Petroleum-bearing fluid inclusions were observed in very low abundances in two of the eight samples studied for fluid inclusions (1855.50 m in 7128/4–1 and 2076.00 m in 7128/6–1); none were present in the other six samples. These inclusions are secondary, occupying healed microfractures or trapped between quartz crystals. None were suitable for measurement of homogenization temperature. All fluoresced green-blue, suggesting a light oil composition, probably over 40°API gravity (Sellwood et al. 1993).

Primary aqueous inclusions were measured in coarse carbonate cements from four samples (Fig. 13). No data were obtained from finely crystalline carbonate cements and coarse anhydrite owing to lack of suitable inclusions. Two types of primary aqueous inclusions were observed: monophase liquid, and two-phase liquid-rich. Monophase inclusions occur in rare very coarse calcite crystals (possibly syntaxial overgrowths on echinoderm fragments) at 2076 m in 7128/6–1 and in petrographically early, inner regions of crinoid overgrowths in the calcareous sandstone at 1814.5 m in 7128/4–1. Monophase inclusions are believed to indicate trapping temperatures of $< 50°C$ (Goldstein and Reynolds 1994).

Homogenization temperatures (T_h) of two-phase inclusions from all minerals range from 52 to 117°C (Fig. 13), suggesting essentially continuous cementation over a wide temperature range. In general, average T_h values are higher for cement types that appear petrographically to have formed later. Thus in sample 1814.5 m from 7128/4–1, quartz cement predates

most calcite cement, which predates scattered dolomite rhombs, consistent with the sense of increasing T_h values of these cements (Fig. 13D). In samples 2075.00 and 2076.00 m from 7128/6–1, coarse calcite predates saddle dolomite, consistent with higher average T_h of the latter (Fig. 13A). Anhydrite in these samples occurs mainly as coarse crystals that appear petrographically later than the coarse calcite spar, and yet T_h values from anhydrite are mainly lower than values from the coarse calcite. This seeming anomaly is accounted for by the observation that the inclusion-bearing anhydrite consists of subordinate areas of relatively fine crystal size, which may represent an early anhydrite generation. Similarly, the monophase inclusions in very coarse calcite (Fig. 13A) probably reflect early growth of this suspected syntaxial overgrowth cement, relative to the volumetrically dominant coarse–blocky calcite spar.

Salinities are mostly between 15 and 20 wt. % NaCl equivalent (4–6 times seawater salinity) regardless of the mineral host. Two exceptions are: (1) salinities of 6–7 wt. % (twice seawater salinity) in the innermost zone of calcite overgrowths on crinoid fragments in the L-7 sandstone and (2) salinities of 21–25 wt % (6–7 times seawater salinity) in the rare very coarse calcite in sample 2076 m from unit L-2.

Cement Stable-Isotope Compositions

Microsampled calcite analyses are classified as matrix + bioclasts, fine spar, or coarse spar. Figure 14A shows that the coarse spar has generally lower oxygen isotope values than matrix and fine spar. Furthermore, the zoning sequence within late spar areas tends to progress toward more negative $\delta^{18}O$ with time (Fig. 14A). Coarse spar compositions also extend to lower $\delta^{13}C$ values compared with fine spar and matrix.

The dolomite analyses are classified as fine dolomite, coarse dolomite, or saddle dolomite. Analyses were also made of Fe-rich saddle dolomite (?ankerite) cement filling intergranular porosity and veins in a core sample of the metasandstone basement from well 7128/6–1 (2540.50 m depth). Figure 14B shows that the coarse dolomites have a quite limited range of $\delta^{18}O$ (-5 to $-6.5‰$), whereas fine dolomites have a wider range, extending to much higher values ($+3.5$ to $-5‰$). The saddle dolomites partly overlap with the coarse dolomites, but extend to lower values (predominantly -5 to $-13‰$). Carbon isotope values of the coarse dolomites also have a limited range, whereas both the fine dolomites and the saddle dolomites extend to more negative values. For both calcite and dolomite, there is clear correlation of less positive $\delta^{13}C$ with deeper stratigraphic level (Fig. 15), which is also apparent in the whole-rock data (Fig. 3).

INTERPRETATIONS

Pore Water Evolution

Formation waters at the time of deposition probably consisted of variable marine to hypersaline compositions. Original dominance of normal-marine pore water is attested by the diverse biota comprising most samples throughout the succession. Locally hypersaline conditions are indicated by the occurrence of dolomitic mudstone–wackestone with anhydrite–silica nodules comprising several intervals and by the presence of anhydrite beds 1.5–8 m thick (Ehrenberg et al. 1998a; Ehrenberg et al. 2000a). Significant influence of meteoric water during early diagenesis is consistent with pervasive dissolution of aragonitic bioclasts, frequent inferred exposure surfaces, and the oxygen isotope data discussed below.

Fluid-inclusion data (Fig. 13) indicate that the above pore waters were replaced by waters far more saline than seawater (3.5 wt. % NaCl equivalent) before burial cementation began. The absence of any fluid-inclusion evidence for normal-marine or meteoric waters, despite the pervasive negative oxygen isotope signature in early cements and rock matrix, probably reflects the restriction of our fluid-inclusion data to late, coarse cements. Additional fluid-inclusion data from coarse cements throughout the upper Paleozoic section show a gradient of increasing average salinity with depth,

TABLE 3.—*Average microprobe analyses of different petrographic categories and cement zones from well 7128/6–1.*

Depth (m)	ID[1]	N[2]	CaO (wt.%)	MgO (wt.%)	Fe (ppm)	Mn (ppm)	Sr (ppm)	S (ppm)	Na (ppm)	Si (ppm)	$Mg/CaCO_3$[3] (mol%)	$FeCO_3$ (mol%)	$MNCO_3$ (mol%)
CALCITE:													
1891.75	F	5	54.44	0.53	176 (204/0–477)	146 (201/0–399)	211 (279/0–570)	357 (267/0–610)	790 (395/257–1321)	0 (0/0–0)	1.34 (0.4/0.8–1.8)	0.03	0.03
1902.00	F	9	55.14	0.64	103 (160/0–451)	83 (164/0–381)	104 (201/0–594)	379 (135/193–551)	234 (234/0–567)	20 (46/0–137)	1.58 (1.0/0.9–4.0)	0.01	0.02
1972.00	F	4	55.96	0.46	91 (140/0–295)	84 (67/11–150)	0 (0/0–0)	373 (47/327–430)	91 (127/0–270)	25 (50/0–99)	1.14 (0.2/0.1–1.3)	0.02	0.02
1976.00	F	6	55.82	0.52	104 (123/0–291)	61 (111/0–276)	29 (71/0–173)	465 (239/170–737)	120 (213/0–534)	52 (128/0–314)	1.28 (0.3/1.0–1.6)	0.02	0.01
1877.25	CIA	16	55.60	0.09	114 (167/0–627)	126 (155/0–497)	6 (25/0–103)	66 (79/0–221)	68 (106/0–326)	0 (0/0–0)	0.22 (0.1/0.1–0.5)	0.02	0.02
1877.25	C1	44	55.12	0.39	385 (306/0–961)	154 (180/0–895)	40 (127/0–545)	73 (80/0–237)	170 (258/0–827)	0 (0/0–0)	0.98 (0.2/0.4–1.2)	0.07	0.03
1877.25	C2	11	54.93	0.46	56 (99/0–321)	346 (149/48–515)	33 (62/0–183)	22 (48/0–156)	106 (196/0–527)	0 (0/0–0)	1.16 (0.1/1.0–1.3)	0.01	0.06
1877.25	C3	41	54.79	0.45	797 (331/0–1435)	129 (125/0–520)	55 (199/0–951)	66 (89/0–292)	86 (184/0–968)	10 (66/0–423)	1.13 (0.1/0.9–1.5)	0.14	0.02
1960.00	M	16	54.51	0.83	66 (102/0–266)	71 (110/0–304)	292 (228/0–588)	537 (170/289–931)	872 (391/67–1628)	1173 (1053/184–4431)	2.06 (0.2/1.8–2.5)	0.01	0.01
1960.00	F	4	54.78	0.91	74 (115/0–242)	34 (68/0–136)	484 (208//197–692)	603 (469/14–1077)	336 (229/0–491)	502 (533/0–1022)	2.25 (0.8/1.5–3.3)	0.01	0.01
1960.00	CIA	5	56.57	0.17	1 (2/0–5)	85 (114/0–274)	94 (209/0–468)	58 (55/0–111)	312 (122/164–438)	0 (0/0–0)	0.41 (0.0/0.4–0.5)	0.00	0.02
1960.00	C1	28	55.80	0.43	152 (163/0–587)	84 (94/0–283)	326 (1150/0–6132)	179 (1540/0–510)	239 (307/0–937)	142 (547/0–2878)	1.05 (0.2/0.5–1.5)	0.03	0.02
1960.00	C2	3	55.60	0.45	365 (140/228–508)	287 (161/183–473)	9 (11/0–21)	27 (24/0–45)	365 (417/75–842)	0 (0/0–0)	1.12 (0.0/1.1–1.1)	0.07	0.05
1960.00	C3	50	55.73	0.43	531 (185/160–991)	170 (165/0–592)	50 (94/0–395)	63 (80/0–319)	359 (338/0–1210)	6 (36/0–255)	1.07 (0.1/0.9–1.3)	0.09	0.03
2076.00	F*	9	54.60	1.12	369 (607/0–1613)	116 (149/0–388)	62 (124/0–357)	855 (342/140–1257)	245 (275/0–727)	13 (30/0–87)	2.77 (0.8/1.6–3.9)	0.07	0.02
2122.00	F	26	54.07	0.71	407 (432/0–1508)	749 (485/0–1786)	37 (106/0–445)	850 (1110/68–5732)	1011 (811/0–4003)	357 (1471/0–7321)	1.79 (0.6/0.9–3.3)	0.07	0.14
2122.00	C1	22	54.99	0.29	551 (273/130–1069)	816 (443/224–2304)	52 (113/0–449)	155 (94/0–331)	478 (396/0–1180)	6 (26/0–121)	0.72 (0.3/0.4–1.2)	0.10	0.15
2122.00	C2	17	54.42	0.24	1540 (462/676–2842)	2522 (538/1492–4041)	59 (135/0–521)	180 (112/0–381)	346 (290/0–878)	0 (0/0–0)	0.61 (0.3/0.5–1.6)	0.28	0.47
2122.00	C3	7	53.30	0.56	7203 (935/5515–8071)	1852 (369/1285–2280)	85 (151/0–368)	61 (49/0–148)	578 (537/0–1262)	0 (0/0–0)	1.43 (1.1/1.3–1.6)	1.32	0.34
2122.00	C4	49	52.96	0.46	3589 (977/2002–6970)	1560 (459/649–2915)	45 (174/0–1115)	145 (124/0–448)	937 (1303/0–7969)	1 (9/0–66)	1.17 (0.3/0.5–1.6)	0.67	0.29
DOLOMITE:													
1891.75	F	1	31.58	20.42	894	150	0	296	437	307	52.56	0.15	0.03
1902.00	F	4	31.99	20.25	5740 (6313/356–12542)	174 (22/0–494)	0 (0/0–0)	74 (86/13–200)	82 (23/55–102)	0 (0/0–0)	52.65 (0.3/52.4–53.1)	0.96	0.03
1911.25	F	4	32.27	20.72	1562 (447/1157–2137)	71 (94/0–199)	0 (0/0–0)	436 (112290–543)	334 (405/57–935)	840 (1468/0–3030)	52.69 (0.5/52.1–53.1)	0.26	0.01
1915.00	F	4	32.32	20.89	1372 (444/804–1744)	81 (121/0–259)	65 (131/0–261)	262 (104/120–368)	291 (336/0–622)	287 (378/0–798)	52.53 (0.3/52.1–52.8)	0.22	0.01
2024.00	F	4	31.74	20.51	4896 (1370/3337–6115)	184 (89/109–308)	189 (378/0–755)	785 (425/326–1260)	671 (199/444–906)	1610 (13115/0–3154)	52.23 (0.5/51.8–52.8)	0.81	0.03
2047.00	F	18	32.33	19.78	7446 (6577/1286–16176)	135 (180/0–380)	42 (107/0–354)	816 (891/4–1852)	609 (719/0–1535)	352 (704/0–1408)	53.35 (1.8/50.8–54.9)	1.24	0.02
1976.00	C1	6	32.91	20.74	385 (251/0–738)	59 (107/0–403)	72 (117/0–289)	208 (188/0–721)	196 (254/0–953)	610 (43/0–183)	53.25 (0.6/52.3–54.5)	0.06	0.01
1976.00	C2	2	32.41	20.05	5691 (1255/4669–7695)	319 (442/0–1193)	0 (0/0–)	116 (42/56–167)	157 (125/0–327)	0 (0/0–0)	53.22 (0.3/53.0–53.7)	0.94	0.05
1976.00	C3	22	32.66	20.90	558 (383/287–828)	246 (342/4–488)	40 (120/0–532)	0 (0/0–0)	32 (45/0–64)	0 (0/0–0)	52.84 (0.1/52.8–52.9)	0.09	0.04
1976.00	S		32.03	19.95	10018 (397/9289–10964)	308 (171/0–603)		91 (78/0–276)	101 (148/0–448)	16 (53/0–230)	52.67 (0.3/51.9–53.4)	1.65	0.05
1976.00	S	1	31.98	19.88	9093		0	0	236	0	52.82	1.51	0.00
2077.00	S	6	32.45	14.96	51202 (5749/43104–58631)	1205 (175/974–58631)	152 (144/0–360)	77 (100/0–267)	241 (337/0–744)	0 (0/0–0)	55.45 (0.9/54.3–56.7)	8.78	0.21

Average values are followed by (standard deviation/minimum-maximum).
[1] ID = petrographic category: M = matrix; F = fine spar; C = coarse spar (with zones numbered); S = saddle dolomite; F* = earliest nonluminescent fine spar zone; CIA = very low-Mg portion of coarse spar Zone 1.
[2] N = number of analyses averaged.
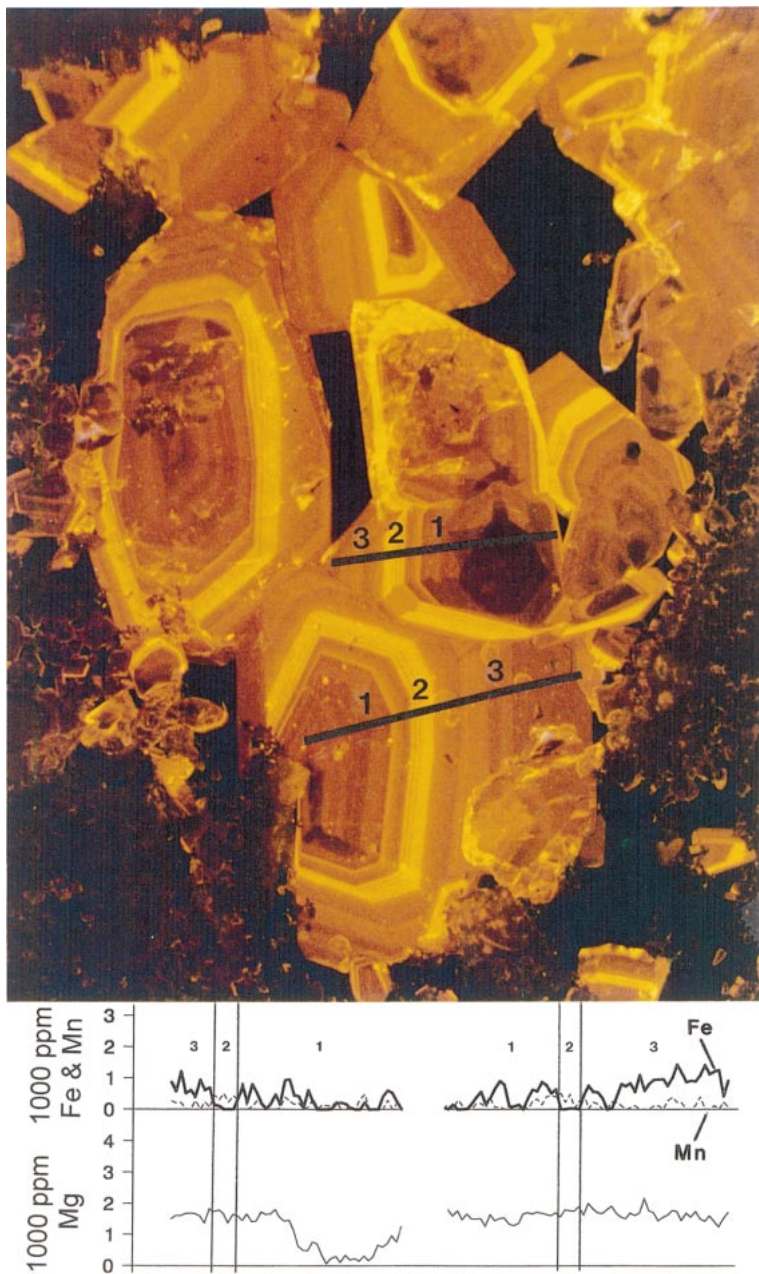[3] $MgCO_3$, mol% given for calcite. $CaCO_3$ mol% give for dolomite.

FIG. 8.—Cathodoluminescence photo showing calcite cements infilling the interior of a mold in a buildup at 1877.25 m core depth in well 7128/6–1 (unit L-6). Black areas between crystals at mold center are pores. Lines show paths of two microprobe traverses. Profiles of Fe, Mn, and Mg are plotted below at the same horizontal scale as the traverse line in the photo (upper traverse at left), with cement zones labeled as on photo: 1 = coarse spar zone 1; 2 = coarse spar zone 2; 3 = coarse spar zone 3. In each traverse, zones 1, 2, and 3 are from a single crystal. Note that zone 1 in the first (upper) traverse includes an early nonluminescent zone of very low-Mg composition.

from 11–14% at 1.6 km depth in unit L-9 to 18–23% at nearly 2.5 km in Visean sandstones (Fig. 16). This suggests a stratified water column at the time of burial cementation. The composition of present formation water is uncertain but appears to be highly saline. Water sampled from a drill-stem test in the spiculite reservoir (top of unit L-9) in well 7128/4–1 was highly contaminated with mud filtrate during drilling but contained around 14 wt. % total dissolved solids.

Two alternative models for the origin of the stratified high-salinity brine column indicated by Figure 16 are: (1) southward lateral brine flow from upper Carboniferous to lower Sakmarian evaporite-bearing strata nearer the evaporitic Nordkapp basin (Fig. 1) and (2) brine emplacement by a series of reflux events at successive stages of platform deposition, followed by compactionally driven upward displacement of high-salinity waters into units L-6 through L-9. A third model, involving derivation of the high-salinity brines by upward migration from deeper, pre–Upper Carboniferous strata, may be rejected as implausible because the Lower Carboniferous siliciclastic section in this area contains no known evaporite beds and was deposited under conditions ranging from nonmarine (fresh water) to near-shore marine (normal seawater).

Model 1 above is generally plausible but cannot readily account for the observed salinity stratification of the water column. Model 2 can explain this stratification as the product of multiple reflux events. Deeper strata would have experienced more reflux events, resulting in higher salinity content because of more complete displacement of original lower-salinity pore waters. Decreased prevalence of hypersaline conditions beginning in mid-Asselian time is indicated by marked decrease in dolomite and anhydrite abundance upwards from the base of unit L-6. Evaporitic conditions then ended completely in mid-Sakmarian time, corresponding with the base of unit L-8. Thus units L-6 to L-9 would have been deposited containing mostly normal-marine porewaters. However, these waters would have been partly replaced by hypersaline waters driven upwards through the section by compaction during subsequent burial.
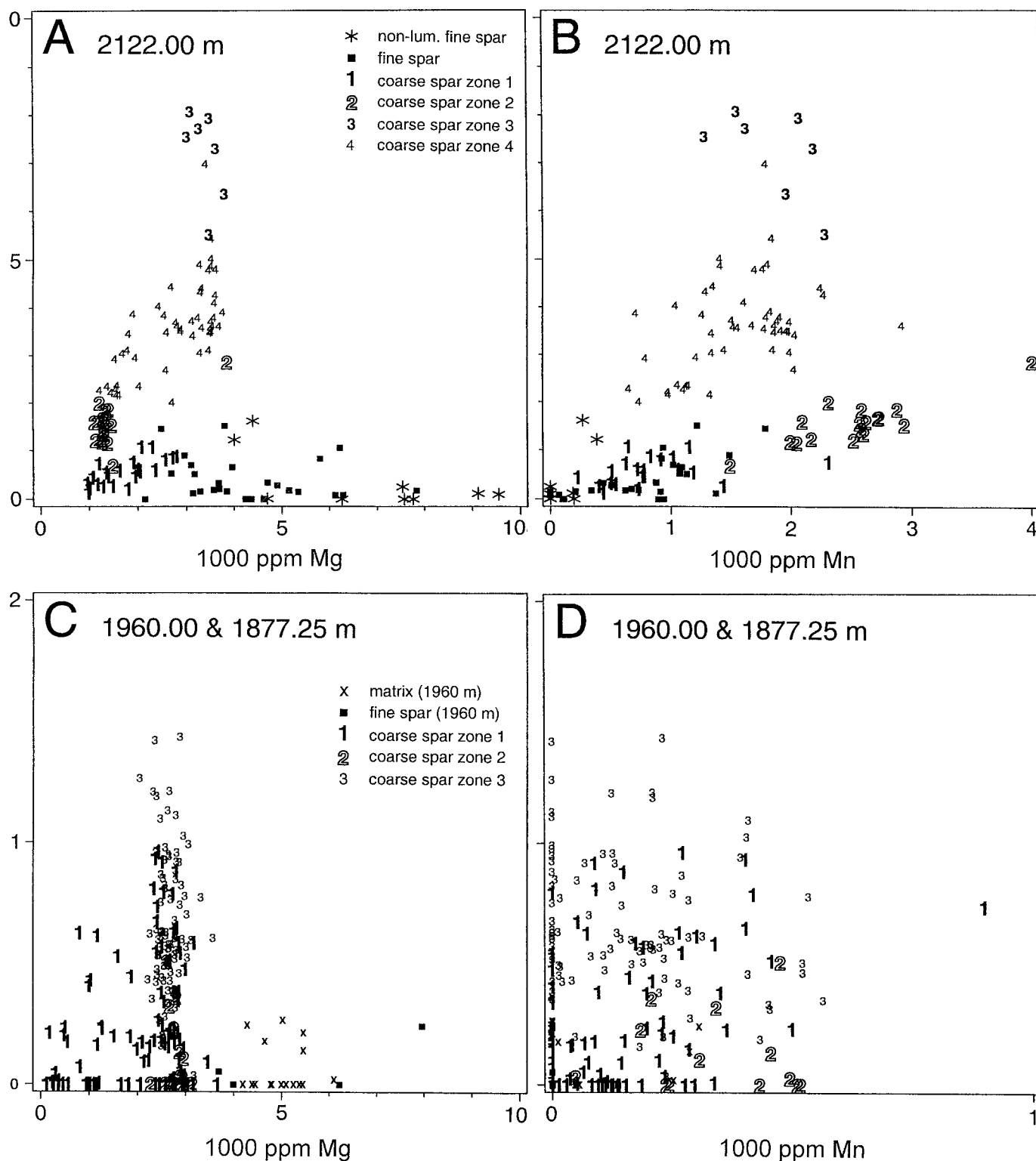
FIG. 9.—Microprobe analyses of calcites. **A, B)** Sample 2122.00 m in well 7128/6–1 (profile illustrated in Fig. 6) and earliest, nonluminescent zone of prismatic fine spar in sample 2076.00 m (ID = F* in Table 3). **C, D)** Samples 1960.00 and 1877.25 m in well 7128/6–1 (illustrated in Figs. 7 and 8).
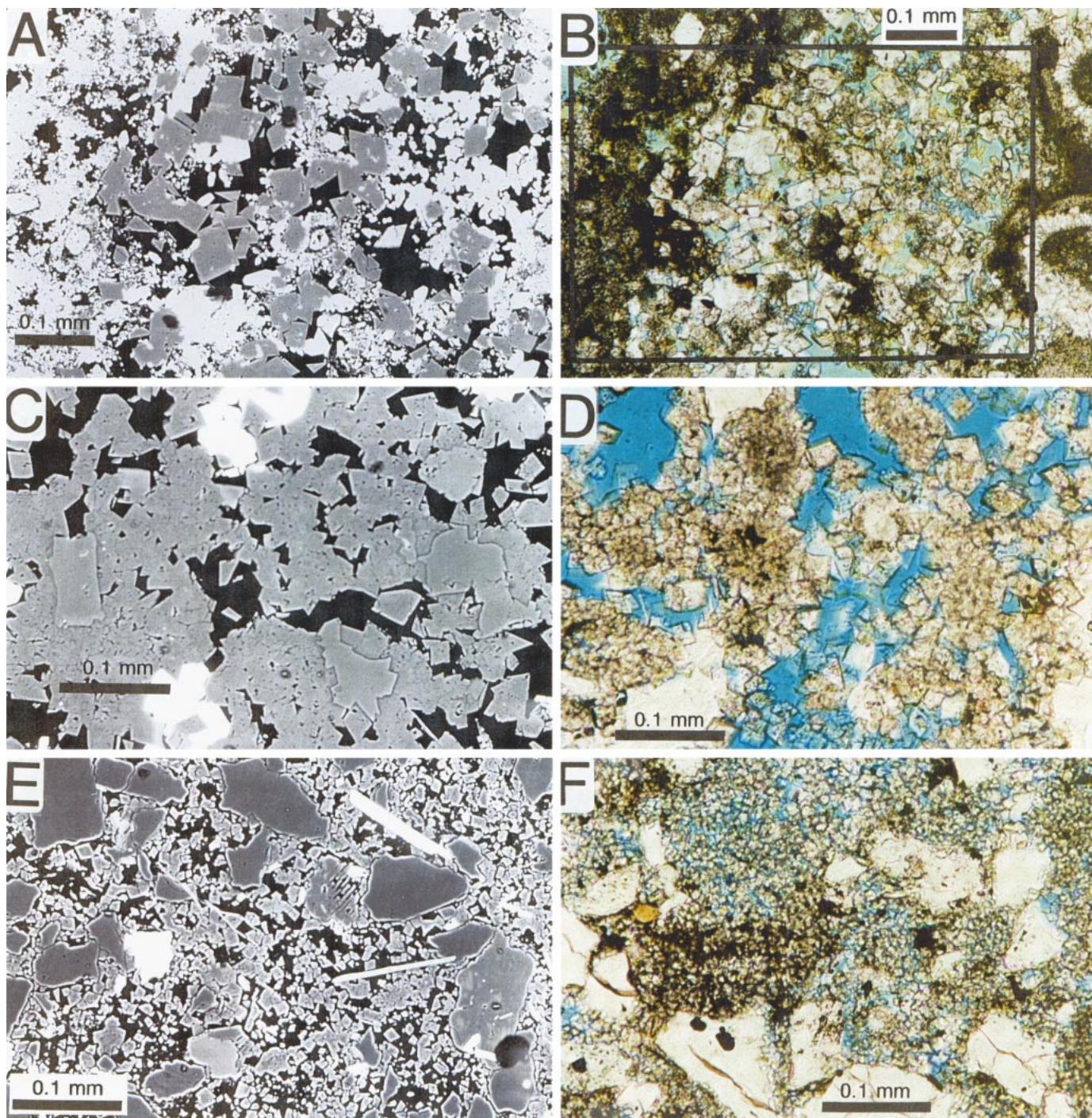
FIG. 10.—Backscattered-electron (BSE) images (left) and photomicrographs (right) showing the variable petrographic characteristics of fine dolomite in three samples from well 7128/6–1. (2024.00, 1915.00, 1901.00). **A, B)** Fine dolomite both replaces calcite microspar matrix and infills matrix porosity in a foraminifera grainstone from 1901.00 m core depth (base of unit L-6). In the BSE image, black is porosity; light gray is calcite; and dark gray is dolomite. Rectangle in photomicrograph outlines exact area of BSE image. **C, D)** A dolomitic mudstone from 1915.00 m (unit L-5). Fine dolomite includes both anhedral-turbid microdolomite and coarser cement crystals that have euhedral-clear (''limpid'') rims. Dolomite is enclosed in later anhydrite and celestite cements (white on BSE image). **E, F)** A dolomitic mudstone from 2024.00 m (unit L-3). This example of fine dolomite includes only very fine microdolomite (no cement crystals as large as the coarser crystal size in sample 1915.00), but both anhedral-turbid and euhedral-clear crystal varieties are present.
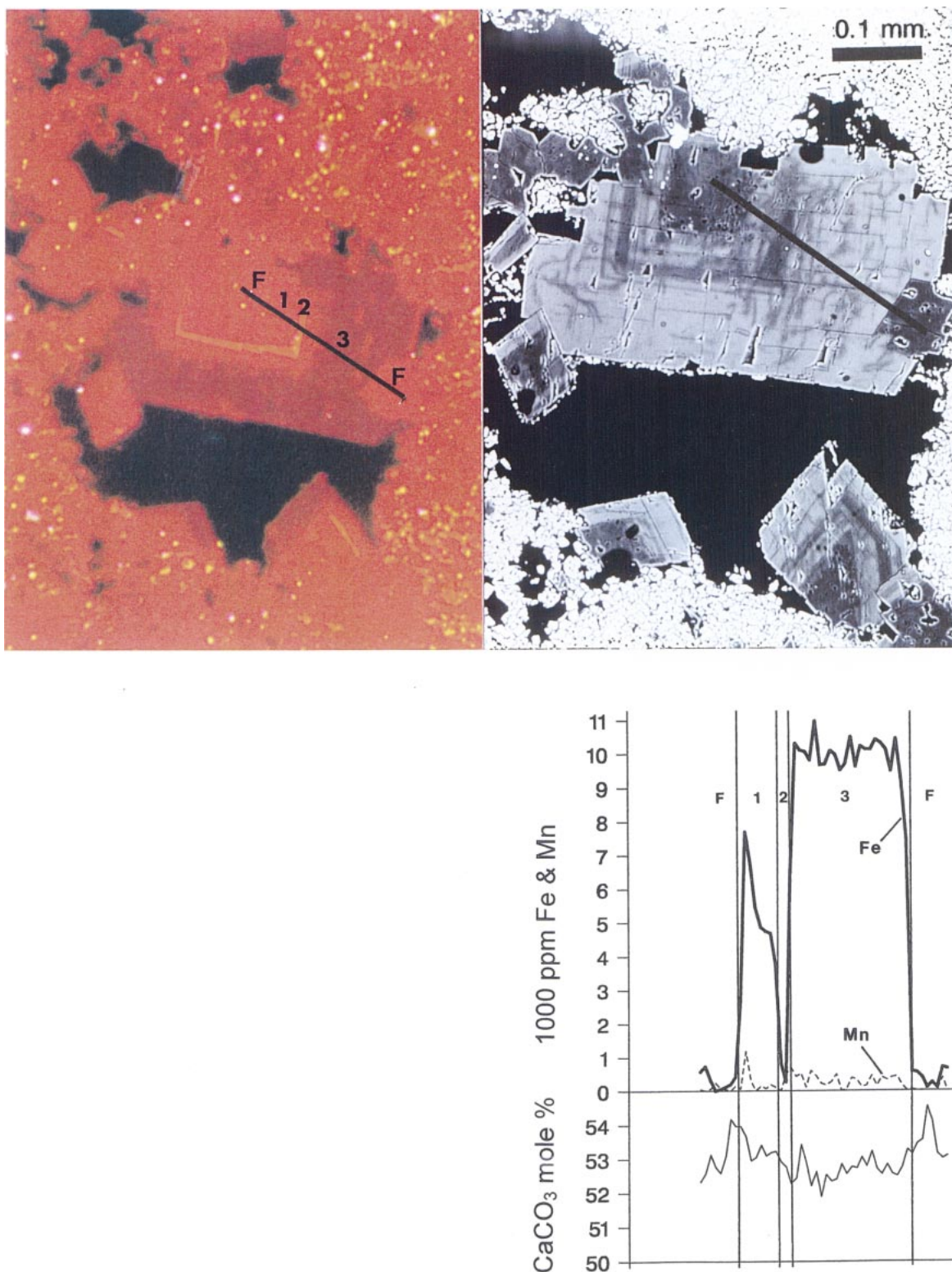
FIG. 11.—Cathodoluminescence (left) and BSE (right) images of approximately the same area, showing fine and coarse dolomite cements infilling a moldic pore in a buildup at 1976.00 m core depth in well 7128/6–1 (unit L-4). Pore walls consist of calcite microspar (originally mud matrix). Lines show path of microprobe traverse. Profiles of Fe, Mn, and Ca are plotted below at the same horizontal scale as the traverse line in the photo, with cement zones labeled as on CL photo: F = fine spar; 1 = coarse spar zone 1 (moderate CL); 2 = coarse spar zone 2 (thin bright-CL layer); 3 = coarse spar zone 3 (dull-CL).
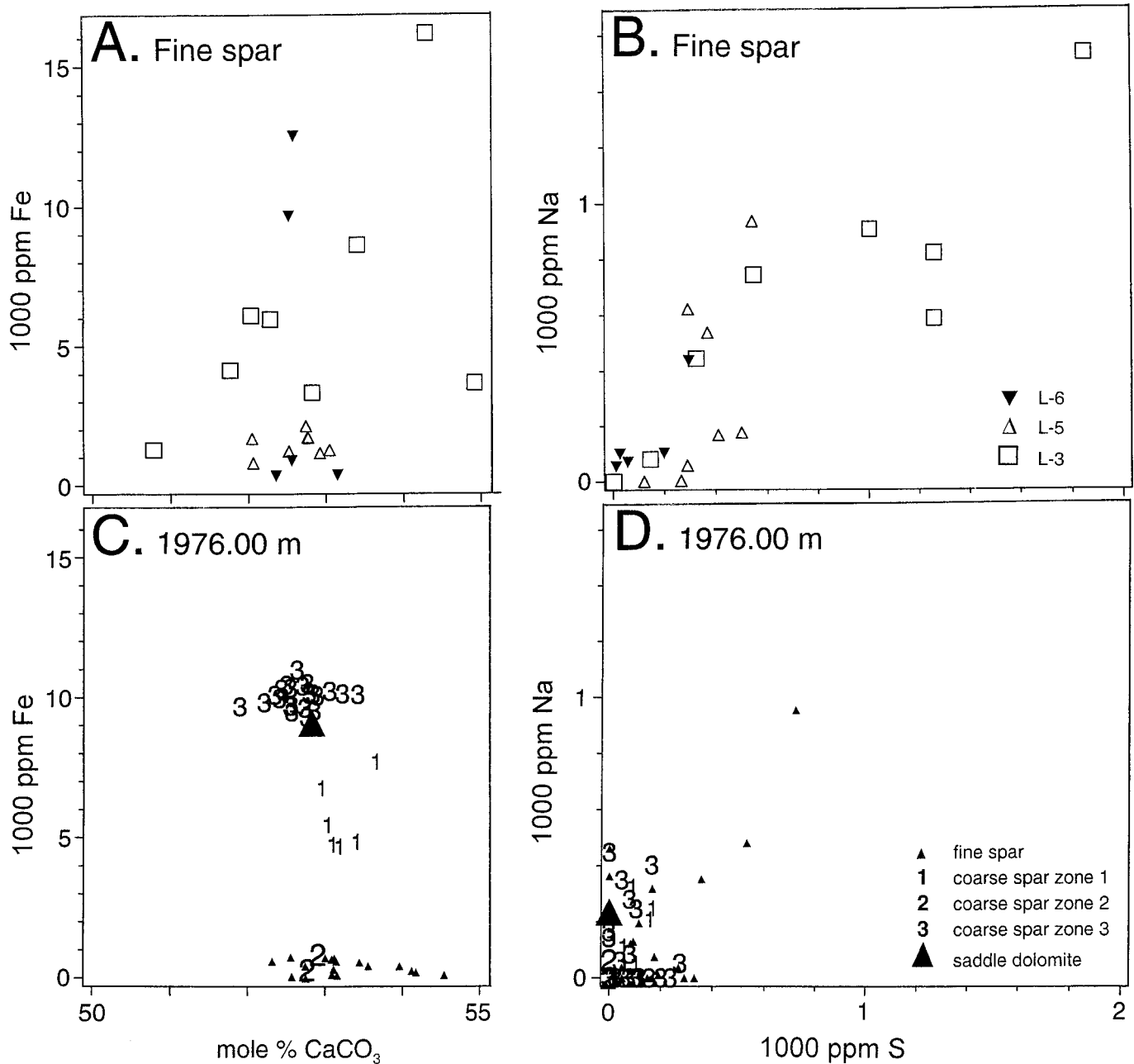
FIG. 12.—Microprobe analyses of dolomites. **A, B)** Fine spar compositions from six samples (illustrated in Fig. 10) in units L-6 (1891.75 and 1902.00 m); L-5 (1911.25 and 1915.00 m); and L-3 (2024.00 and 2047.00 m). **C, D)** Dolomite cements from sample 1976.00 m (illustrated in Fig. 11).

Judging from the observed values (Fig. 16), the refluxing brines must have had salinities far higher than gypsum saturation (12 wt. %), probably at or near halite saturation (26.5 wt. % at 30°C). A likely source for refluxing halite-saturated brines is during the early-transgressive stages following major lowstands of relative sea level, when the inner platform setting of well 7128/6–1 would have been inundated by hypersaline waters from the Nordkapp Basin.

Whole-Rock-Carbonate Stable Isotopes

Oxygen.—Calcite precipitated in equilibrium with seawater is interpreted to have had values of −3 to −1‰ in the Late Carboniferous and −3

to +1‰ in Permian time (Grossman 1994; Mii et al. 1999). The higher Permian values reflect both local evaporative enrichment of ^{18}O and sampling from high paleolatitudes and thus colder ocean waters. In the Barents Sea, pre-mid-Sakmarian limestones are characterized by warm-water depositional conditions and are therefore expected to have formed from seawater typical of lower latitudes, resulting in depositional $\delta^{18}O$ values in the range −3 to −1‰. The fact that $\delta^{18}O^{WRC}_C$ values for the Finnmark Platform strata are commonly more negative than −4‰ PDB (Fig. 3) indicates either substantial meteoric water influence, abundant late carbonate cements precipitated at elevated temperatures (Land 1983), or both. Both of these factors are thought to be important, on the basis of the inference of repeated subaerial exposure throughout the succession and the
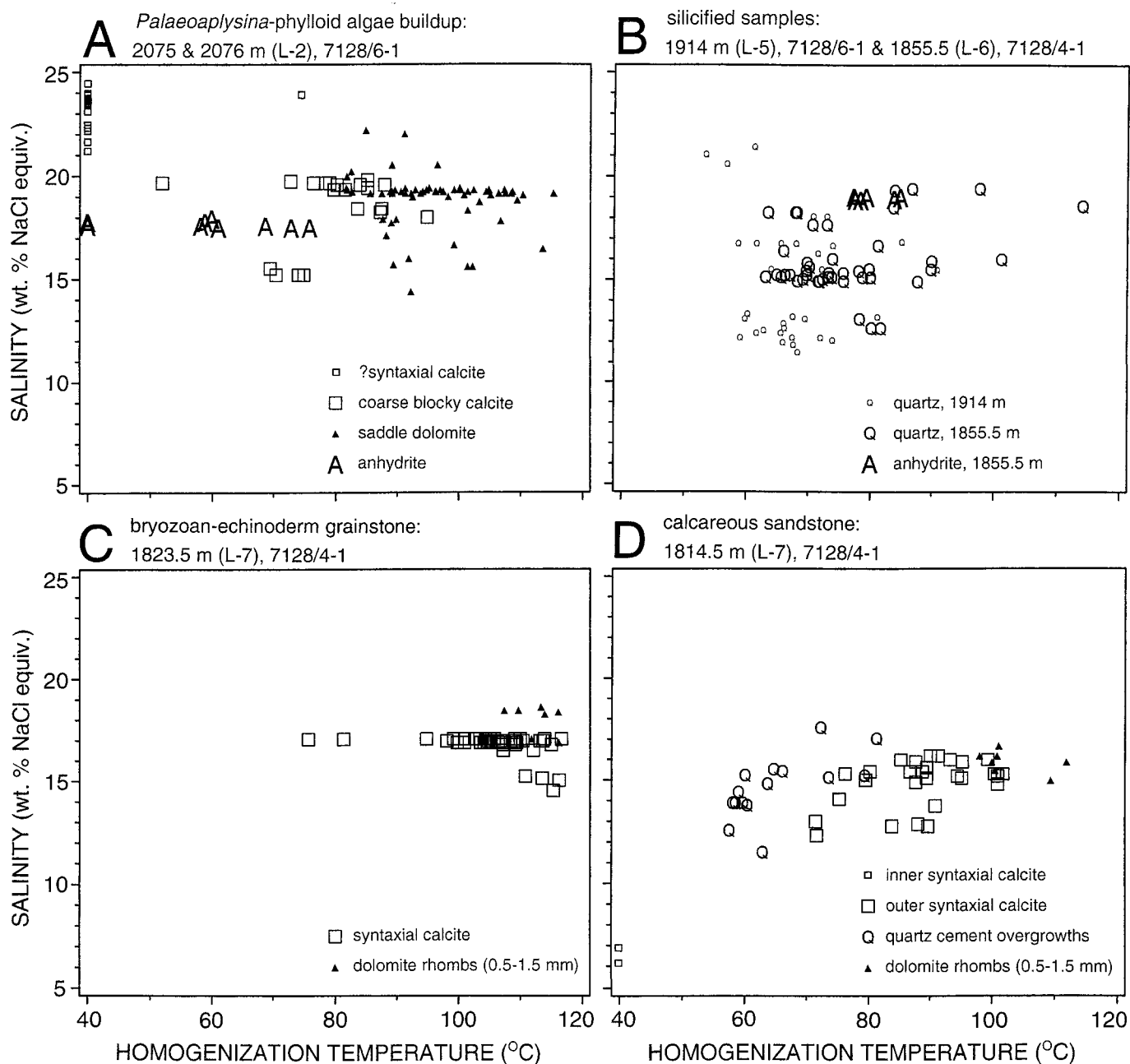
FIG. 13.—Salinity versus homogenization temperatures of primary aqueous fluid inclusions. Monophase inclusions are plotted at 40°C so that salinity data can be shown. Seawater has salinity of 3.5 wt. % NaCl equivalent.

variable abundance of coarse, presumably mesogenetic cements observed in thin section. Their relative contributions are expected to vary widely from sample to sample.

Thin intervals with relatively higher $\delta^{18}O^{WRC}{}_C$ values (-2 to 0‰) stand out as positive excursions in the oxygen isotope profiles. These values have two likely explanations. Many of these samples are low-porosity, undolomitized limestones wherein the relatively positive $\delta^{18}O^{WRC}{}_C$ may represent preservation of primary marine-carbonate values. Other intervals with relatively high $\delta^{18}O^{WRC}{}_C$ consist of dolomitic mudstone or sandstone, for which evaporative enrichment of ^{18}O can be suspected. Other dolomitic mudstone intervals, specifically in unit L-5 and the uppermost part of L-3 (Fig. 2), show distinctly negative displacement of $\delta^{18}O^{WRC}{}_C$, possibly indicating involvement of meteoric water during dolomitization.

Throughout most of units L-6 and L-7, $\delta^{18}O^{WRC}{}_C$ values in well 7128/4–1 are systematically lower by 1 to 1.5‰ than in 7128/6–1 (Fig. 4). This difference could reflect greater volumes of coarse, mesogenetic calcite cement precipitated at elevated temperatures (and thus having relatively negative $\delta^{18}O$) in well 7128/4–1, corresponding with the observed lower porosity relative to the 7128/6–1 section (Fig. 2). An exception to this overall inter-well difference is the two thin beds of dolomitic mudstone in the lower part of L-6 in well 7128/4–1, where evaporative enrichment of $\delta^{18}O$ in a restricted lagoonal setting is a possible explanation for these local positive departures from the surrounding $\delta^{18}O^{WRC}{}_C$ trend.

Carbon.—The range of $\delta^{13}C^{WRC}$ in the carbonate-dominated units L-4 through L-8 (mainly $+4$ to $+6$‰; Fig. 3), is similar to values inferred for Late Carboniferous through middle Permian seawater (Given and Lohmann
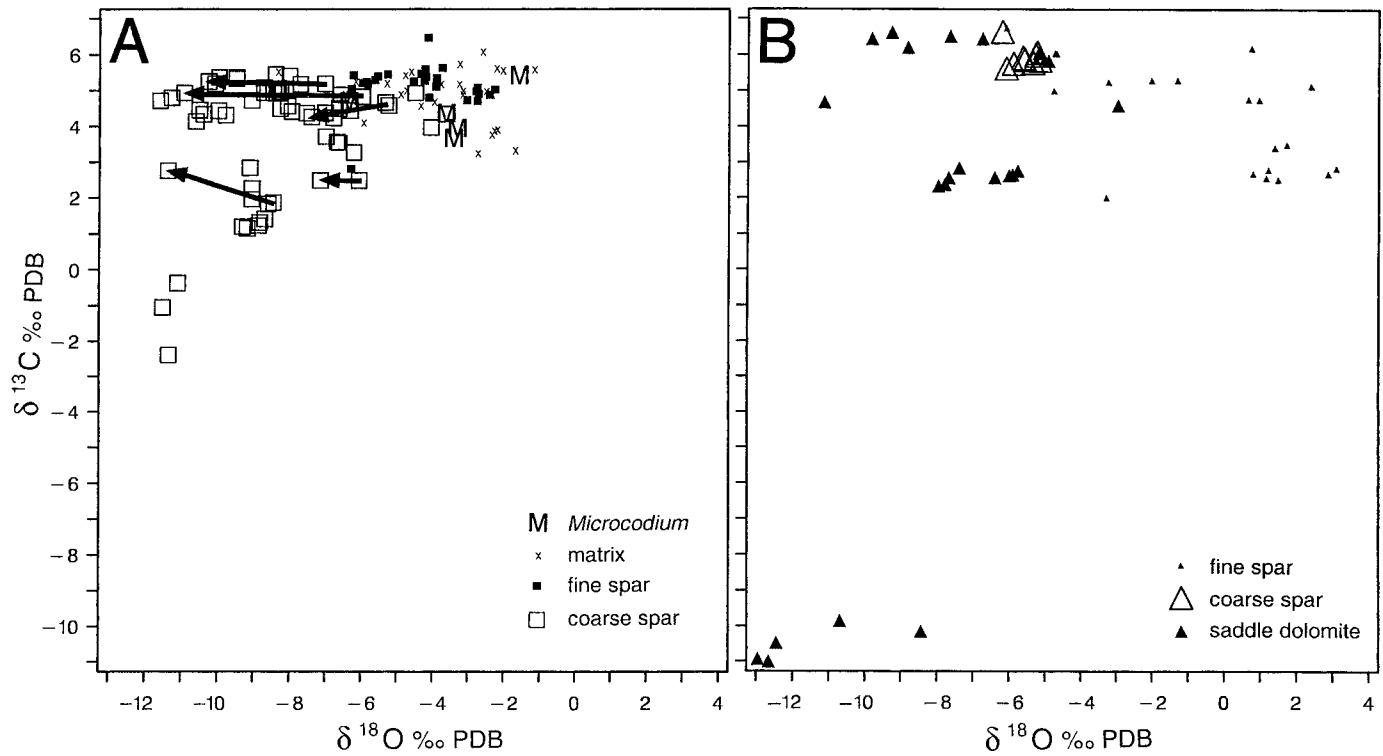
FIG. 14.—Carbon versus oxygen isotope compositions of microsamples from polished thin sections. **A)** Calcite. Arrows indicate direction of isotope change in cases where sequences of multiple analyses from zoning sequences were established by CL petrography. **B)** Dolomite.

1985; Grossman 1994; Scholle 1995), consistent with derivation of the carbon in units L-4 to L-8 mainly from original carbonate sediment and any marine cement present. However, the lower $\delta^{13}C^{WRC}$ range in units L-1 to L-3 (mostly lower than +3.5) indicates exchange with an organic carbon reservoir (Hudson 1977). Assuming values of −25‰ PDB for organic carbon and +6‰ for marine calcite, the observed $\delta^{13}C^{WRC}$ range of mostly 0 to +3‰ (average 2.2‰) in units L-1 and L-2 corresponds with an organic carbon contribution of 24–12% (average 15%). In general, organic carbon incorporated into marine carbonate strata could have been

supplied from four sources: (1) global marine anoxia (Scholle and Arthur 1980); (2) destabilization of methane hydrate deposits (Dickens 1995; Kennedy et al. 2001); (3) development of soil (Allan and Matthews 1982); (4) breakdown of organic matter deposited within the local stratigraphic section; and (5) migration of petroleum.

In the present strata, negative correlation between $\delta^{13}C^{WRC}$ and whole-rock alumina content (Figs. 3, 5) supports the interpretation that the organic carbon was associated with clay content and therefore originated as an intrinsic component deposited within the local stratigraphic section. Clay content in these mixed carbonate–siliciclastic lithologies correlates with decreased energy of depositional conditions, which is in turn expected to correlate with higher organic content in the sediments at the time of deposition. Release of organic carbon from the clay-rich strata may have occurred either eogenetically, during bacterial oxidation and sulfate reduction, or mesogenetically, during thermal maturation and decarboxylation of kerogen (Irwin et al. 1977). Both of these processes may have been important, and their relative magnitude may vary widely from layer to layer. However, the generally low organic carbon content (< 1 wt. %) of even the most aluminous of these rocks, combined with the low post-eogenetic porosity of many of the carbonate lithologies in units L-1 to L-3 (providing little room for late cements to form), argues for a relatively limited role of mesogenetic organic carbon mobilization.

It is surprising and possibly highly significant that negative $\delta^{13}C^{WRC}$ excursions are not observed to be associated with cycle tops and inferred exposure surfaces in the 7128/6–1and 7128/4–1 cores. One of the best-documented mechanisms for incorporation of isotopically negative organic carbon into marine carbonate strata is the downward percolation of waters with isotopically negative bicarbonate ions from a soil horizon (Allan and Matthews 1982). As noted above, numerous surfaces of extended subaerial exposure are believed to be present within this Upper Carboniferous–Lower Permian section, and negative $\delta^{13}C^{WRC}$ excursions are well documented at cycle tops in shallow-water carbonate strata of similar age from other prov-
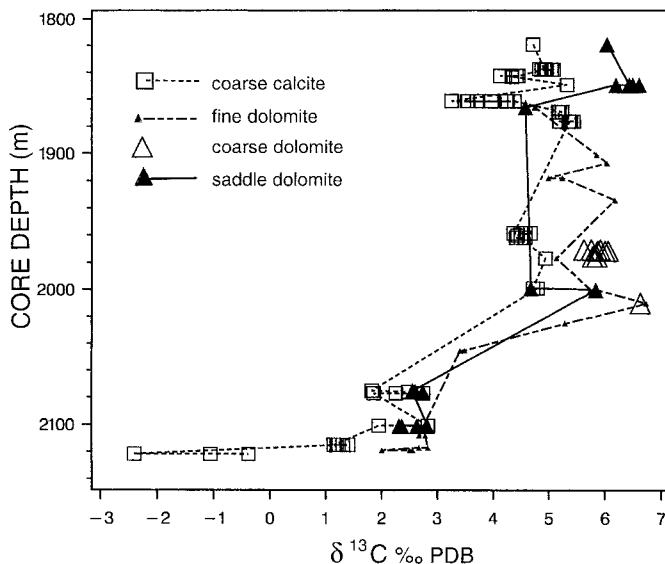

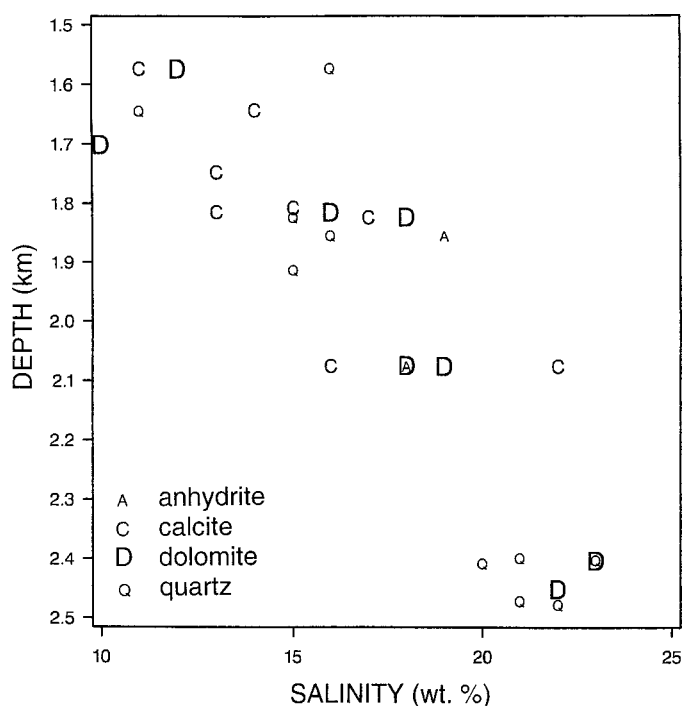FIG. 15.—Depth versus carbon isotope composition of cements.

FIG. 16.—Depth versus salinity (wt. % NaCl equivalent) of primary fluid inclusions in cements in upper Paleozoic strata of wells 7128/4–1 and 7128/6–1. Each point represents the average value measured for the indicated cement in one sample (5–86 measurements per point). Six low-salinity values (3–7 wt. %) forming an outlier group were excluded from one of the quartz samples at 2472 m. Plotting symbol indicates mineral type.
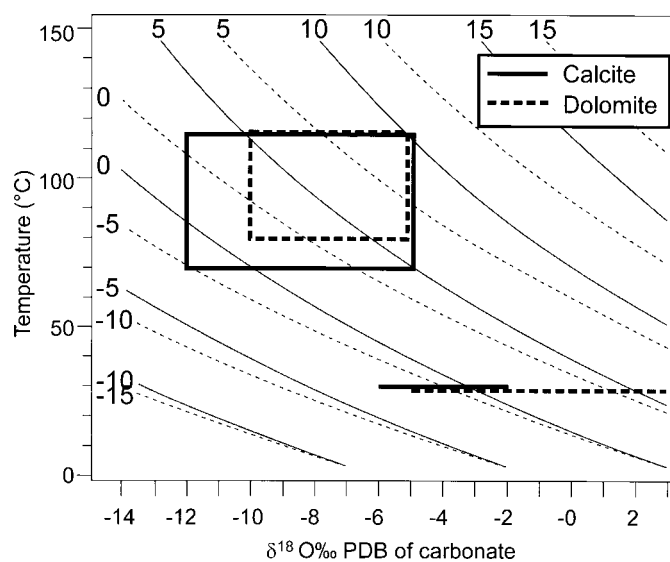

FIG. 17.—Temperature versus $\delta^{18}O$ of calcite and dolomite, with isopleths of equilibrium water composition (‰ SMOW) drawn from equations of O'Neil et al. (1969) for calcite (solid lines) and Land (1983, his fig. 4–2) for dolomite (dashed lines). On each diagram, the horizontal lines at 30°C shows the isotopic range of cements inferred to have formed at near-surface conditions: fine calcite (solid line) and fine dolomite (dashed line). Boxes show the range of temperature (from fluid-inclusion homogenization temperatures (Fig. 13) and isotope composition (Fig. 14) of inferred burial cements: coarse calcite spar (solid box) and coarse and saddle dolomite (dashed box).

inces (Allan and Matthews 1982; Goldstein, 1991; Wagner et al. 1995; Saller et al. 1999; Immenhauser et al. 2000). A possible explanation is that soil-related, negative $\delta^{13}C$ excursions were not developed during exposure of the present strata because of limited vegetation, perhaps reflecting arid climatic conditions. This explanation seems preferable to invoking a general lack of exposure at cycle tops. Another process that could locally account for absence of negative $\delta^{13}C$ excursions is erosion of cycle tops during transgression, but it seems difficult to postulate that this process operated consistently to remove all ^{13}C-depleted cycle tops throughout the succession.

Origin and Timing of Cement Generations

Our model for cementation (Table 2) comprises: (1) an eogenetic stage of fine calcite precipitation from marine to mixed-meteoric waters, locally overprinted by eogenetic dolomitization and calcium sulfate cementation in intervals deposited under restricted, hypersaline conditions, (2) an extended mesogenetic stage of coarse cement growth (calcite and, more locally, dolomite, depending upon Mg supply); and (3) a latest mesogenetic stage of saddle dolomite and anhydrite cementation.

Eogenetic Calcite Cementation.—Fibrous marine cement is rare to absent in the Finnmark carbonates, possibly reflecting both degree of seawater carbonate saturation and the low current energy of this inner-platform setting, where only limited volumes of marine pore water were circulated through the upper sediment column. The most abundant cement of likely marine origin is the micropeloidal calcite, which forms a dominant component of the mud matrix in buildup facies. This cement is likely to be a microbially induced precipitate (Pickard 1996).

Fine calcite cement is interpreted to have originally formed as low-Mg calcite, judging by chemical composition (2000–10,000 ppm or 0.8–4.0 mol% $MgCO_3$, low Fe and Mn, and widely varying but generally high Na,

Sr, and S; Fig. 9 and Table 3), preservation of CL zoning, and absence of microdolomite inclusions. The compositional range indicates growth from variably Mg-rich waters, probably reflecting eogenetic–phreatic cementation involving different mixtures of meteoric water and seawater (Budd and Land 1990; Saller and Moore 1991).

As noted above, estimates for the $\delta^{18}O$ of calcite precipitated directly from Late Carboniferous and Early Permian seawater at warm-water latitudes lie between −3 and −1‰ (Grossman 1994; Mii et al. 1999). Thus the generally more negative values of the fine calcite cements (−2.3 to −6.5‰, but mainly < −3.5‰; Fig. 14A) are consistent with precipitation from meteoric-influenced waters at low temperature. Assuming a surface temperature around 30°C, the $\delta^{18}O$ values of fine spar correspond with water compositions having a range of roughly −3 to +2‰ SMOW (Fig. 17), which is moderately depleted to enriched in ^{18}O relative to estimated Permian seawater composition (−1.4 to 0.0‰, assuming water temperatures of 25–31°C; Given and Lohmann 1985).

The range of marine-calcite $\delta^{13}C$ in Late Carboniferous–Permian time is +5 to +7‰ (Given and Lohmann 1985; Scholle 1995), although values from the central U.S.A. are systematically lower, apparently reflecting restricted oceanic circulation (Grossman 1994; Mii et al. 1999). The slightly lower $\delta^{13}C$ values of the fine calcite cements, +4.5 to +5.5‰ (Fig. 14A), may reflect minor involvement of organic carbon, which might have been present as a primary depositional component of the sediment.

A distinctive type of early calcite cement is *Microcodium*, which has been observed at only one place in the 7128/6–1 cores, at 1886.30 m in unit L-6. *Microcodium* is thought to form as a soil feature surrounding rootlets (Klappa 1978), and therefore provides definitive evidence for a subaerial exposure surface. The minor negative displacement of the *Microcodium* $\delta^{13}C$ values relative to the field of matrix and fine cement values in Figure 13A indicates, however, that the carbon budget in this apparent soil precipitate was dominated by marine-derived carbon from the carbonate sediment matrix. This result is consistent with the apparent absence of

soil-related negative $\delta^{13}C$ excursions in the whole-rock isotope profiles (Fig. 3).

Eogenetic Dolomitization.—The fine dolomite is interpreted to have formed shortly after deposition by replacement of carbonate mud and subsequent near-surface cementation, mainly in low-energy, hypersaline lagoonal to sabkha settings. It is to be expected that the fine dolomites record a complex diagenetic history, as outlined in general terms by Land (1983) for ostensibly similar dolomitic strata from the Cretaceous Edwards Formation of Texas. The wide oxygen isotope range of the fine dolomites (-6 to 3‰; Fig. 14B) probably reflects varying compositions of the waters involved during dolomitization, including both isotopically positive evaporated marine water (McKenzie 1981) and isotopically negative meteoric waters in the ''schizohaline'' environment (Folk and Siedlecka 1974). Isotope values may also have been altered by continued growth of fine dolomite crystals at elevated temperatures, as evidenced in the fluid-inclusion data from the two samples from unit L-7 in well 7128/4–1 (Fig. 13).

Assuming surface temperature around 30°C, the $\delta^{18}O$ range of the fine dolomite corresponds with water compositions in the range -6 to $+2$‰ SMOW (-36 to -28‰ PDB; Fig. 17). The generally low Fe of the fine dolomite, corresponding to overall moderate CL intensity (Pierson 1981; Machel and Burton 1991), probably reflects crystallization under oxidizing conditions near the sediment–water interface, whereas the variably higher Fe values of a subordinate fraction of the fine dolomites (Fig. 12), commonly forming rims on earlier low-Fe cores, suggests recrystallization–overgrowth under subsequent, more reducing conditions.

Mesogenetic Dolomitization.—Coarse dolomite spar is interpreted to be a burial cement because it forms overgrowths around earlier fine dolomite rhombs and has Fe-rich composition (Figs. 11, 12). The relationship in time and space to the coarse calcite spar is problematic, however, because the coarse dolomite and calcite spars only rarely occur associated within the same pore spaces. Samples with abundant coarse dolomite tend to have little coarse calcite and vice versa. Nevertheless, in examples where both cement types are in contact, the coarse calcite encloses coarse dolomite rhombs and thus appears to be the later cement phase. Because no fluid-inclusion data were obtained from coarse dolomite crystals, and the stable-isotope analyses of coarse dolomites are all from a limited depth range (1971–1976 m) in unit L-4, the conditions of coarse dolomite formation are poorly constrained.

Mesogenetic Calcite Cementation.—Coarse spar calcites have a smaller range of Mg content (1000–4000 ppm or 0.4–1.6 mol% $MgCO_3$; Fig. 9) than the fine calcite analyses. These compositions are not indicative of any specific diagenetic setting but have been reported for calcite cements interpreted to have formed from both marine and meteoric connate waters under both eogenetic and mesogenetic conditions (Kaufmann 1997; Grover and Read 1983; Saller and Moore 1991). In samples 1960.00 and 1877.25, however, the coarse spar includes an early zone of relatively pure, low-Mg calcite (0–1000 ppm), similar to compositions formed from meteoric-dominated waters at high water/rock ratios (Dorobek 1987; Meyers 1989; Hendry 1993). Alternatively, these regions of very low Mg content could be an effect of sector zoning (Hendry and Marshall 1991). As observed in many earlier studies (Grover and Read 1983; Dorobek 1987; Kaufmann 1997; Budd et al. 2000), zones with relatively bright CL tend to have high Mn/Fe ratio (Fig. 9).

On the basis of the fluid-inclusion data, the distinctly lower $\delta^{18}O$ of the coarse calcite spar (mainly -5 to -12‰; Fig. 14A) is interpreted as indicating crystallization at elevated temperatures. Using the fluid-inclusion homogenization temperatures and O'Neil et al.'s (1969) fractionation curve, it is possible to calculate that the coarse calcite spar precipitated from pore water having $\delta^{18}O$ somewhere in the range -2 to $+10$‰ SMOW (-32 to -20‰ PDB; Fig. 17). Assuming constant water composition throughout growth of the coarse spar, the zoning trends in Figure 14A (showing decreases in $\delta^{18}O$ by 1–3‰) correspond to temperature increases of roughly 5–15°C during the filling of individual spar-filled vugs (Fig. 17). This sup-

ports the view that the coarse spar formed as temperatures gradually increased during burial.

Early stages of coarse spar growth may represent a continuous transition from the early fine-spar stage, as crystal morphology changed in response to progressive restriction of the fluid system during early burial. Burial cements in deeper stratigraphic horizons may have begun to form at the same time as eogenetic, fine cements were still forming in overlying strata. Coarse spar growth was probably supplied by stylolites within the local stratigraphic environment (Scholle and Halley 1985; Ehrenberg et al. 1998b), so that little or no mass transport over distances greater than a few meters is necessary to explain this volumetrically important porosity-occluding material.

Fe and Mn enrichment at an intermediate stage of coarse calcite cement growth is suggested to have occurred in response to burial diagenesis of clay minerals. Coarse calcite with Fe-Mn-rich zoning occurs mainly within the deeper, relatively clay-rich stratigraphic units L-1 to L-3 (Fig. 6), whereas the calcite cements in overlying shale-poor intervals are Fe-poor throughout their growth history (Figs. 7, 8). Release of Fe and Mn during clay diagenesis has been discussed by Oldershaw and Scoffin (1967), Boles and Franks (1979), McHargue and Price (1982), and Yoo et al. (2000). A popular mechanism is the conversion of smectite to illite, which occurs at temperatures around 80–100°C (Pearson and Small 1988; Deng et al. 1996), but much lower-temperature (< 42°C) release of Fe and Mn from shales has also been documented (Emery 1987). It is uncertain whether the correlation between Fe-Mn-rich composition and shale proximity is also characteristic of the late dolomite cements, because these appear to be Fe-rich throughout the studied intervals (Fig. 11). However, the predominant late dolomite type in the siliciclastic-rich units L-1 and L-2 is extremely Fe-rich saddle dolomite (Table 3), which is rare to absent in the overlying siliciclastic-poor strata.

Development of Fe-Mn-rich zoning also shows overall association with occurrence of relatively low carbon isotope values in both cements (Fig. 15) and bulk carbonates (Fig. 3), indicating a link between clay-rich facies and release of both Fe and isotopically negative, organic-derived carbon. As discussed above, organic carbon is suggested to have been derived from clay-rich beds of the local stratigraphic environment and was released by either eogenetic microbial breakdown or mesogenetic thermal maturation. Thus, the wide $\delta^{13}C$ range of the coarse calcite spar (Fig. 14A) should not be interpreted as an ''L-shaped trend'' reflecting progressive increase in water/rock ratio with decreasing $\delta^{13}C$ (Meyers 1989). A similar correlation between Fe enrichment and lower carbon isotope values has been reported in saddle dolomite cements from Lower Cretaceous carbonates of Texas (Woronick and Land 1985), where it was interpreted as indicating influx from deeper stratigraphic levels of brines rich in both Fe and hydrocarbons. In the Finnmark strata, however, the absence of primary petroleum-filled fluid inclusions suggests that introduction of organic carbon as migrated hydrocarbons was insignificant during growth of carbonate cement.

Saddle Dolomite and Anhydrite.—These associated, coarsely crystalline cements truncate concentric zoning in coarse calcite crystals and therefore represent a distinct latest diagenetic stage. In the two samples where fluid inclusions from both saddle dolomite and coarse calcite were analyzed, T_h values are higher in the saddle dolomite but overlap considerably with the calcite (Fig. 13A). On the basis of these temperature estimates and the oxygen isotope data (Fig. 14B), the saddle dolomite can be estimated to have formed from waters having $\delta^{18}O$ somewhere in the range -2 to $+7$‰ SMOW (-32 to -23‰ PDB; Fig. 17). The geochemistry of the late anhydrite cement has not been addressed in this study, but it is reasonable to envisage an origin involving both remobilization of earlier gypsum or anhydrite within the present strata (Dworkin and Land 1994) and introduction during refluxing of hypersaline brines.

Not all coarse anhydrite is necessarily related to the latest stage of saddle dolomite growth. Many samples, especially in units L-3 through L-5, lack saddle dolomite but contain coarsely crystalline anhydrite and commonly
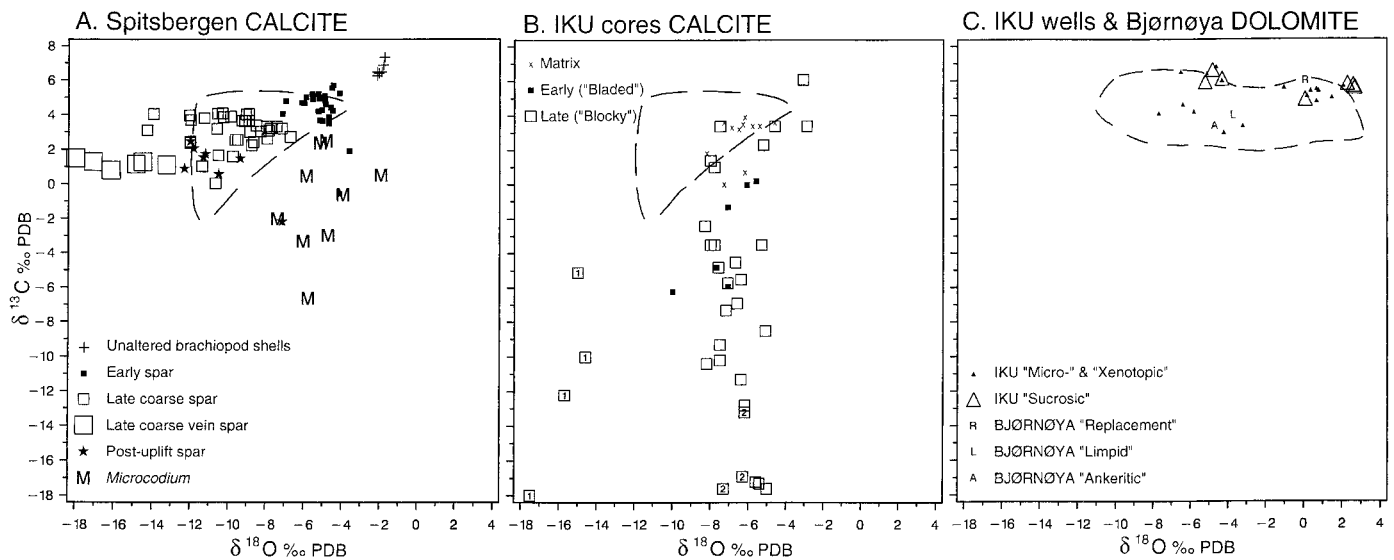
FIG. 18.—Carbon versus oxygen isotope compositions of carbonate cements from Svalbard outcrops and IKU shallow cores. **A)** Calcite compositions from Spitsbergen outcrops (unpublished data of N.A.H. Pickard). Dashed outline shows range of coarse spar compositions from wells 7128/6–1 and 7128/4–1 (Fig. 14A). **B)** Calcite compositions from IKU shallow cores (unpublished data summarized in Stemmerik et al. 1999). Four blocky spar symbols labeled ''1'' are from 126.7 m in well 7030/03-U-01. Three symbols labeled ''2'' are from 19–49 m in well 7029/03-U-02 (possible former petroleum column indicated by vug fillings of calcite spar plus native sulfur). Dashed outline shows range of coarse spar compositions from wells 7128/6–1 and 7128/4–1 (Fig. 14A). **C)** Dolomite compositions from IKU shallow cores and Bjørnøya outcrops (Stemmerik et al. 1993). Dashed outline shows range of all dolomite analyses from wells 7128/6–1 and 7128/4–1, except for the saddle dolomite from the metasandstone basement (Fig. 14B).

also barite showing replacive and/or enclosing petrographic relationships to other minerals.

Saddle dolomite from the 7128/6–1 basement sample may be entirely unrelated to saddle dolomite in the carbonate section several hundred meters above. The highly negative carbon isotope values of the basement dolomite (Fig. 14B) are of interest, however, because they underscore the correlation of more negative carbon with siliciclastic dominance. Carbon in this cement seems unlikely to be derived from marine carbonates because both the host metasediment and the overlying 284 m of Visean sandstone–shale–coal section are nonmarine.

COMPARISON WITH STABLE-ISOTOPE DATA FROM OTHER BARENTS SEA CARBONATE SECTIONS

Carbonate cement stable-isotope data are available from three other areas of the greater Barents Shelf area where carbonate strata correlative with the 7128/6–1 section have been analyzed. These datasets greatly extend the stable-isotope portrait of Barents Shelf carbonates available from the present study (Fig. 18).

Spitsbergen Outcrops

One data set is from outcropping carbonate strata of Moscovian to Asselian age on the island of Spitsbergen, some 850 km north–northwest of well 7128/6–1 (Fig. 1), where similar facies have been studied as analogs to potential exploration targets in the Barents Sea subsurface (Pickard et al. 1996). The Spitsbergen calcite data have a range of variation similar to the present data (Fig. 18A). However, Spitsbergen coarse calcites are offset to moderately less positive δ^{13}C, and a subset of these data, especially late vein-filling spar, extends to considerably more negative δ^{18}O values. Also, compared with the one *Microcodium* sample from 7128/6–1, the Spitsbergen *Microcodium* analyses range toward considerably more negative δ^{13}C, as would be expected for calcite precipitated in soil zones with varying influence of organic carbon. No stable-isotope data have been reported for dolomite cements from Spitsbergen.

Bjørnøya Outcrops

A second data set is from the Asselian Kapp Duner Formation of Bjørnøya, roughly 450 km north–northwest of well 7128/6–1 (Fig. 1). Stemmerik and Larssen (1993) reported average values from three categories of dolomite in completely dolomitized *Palaeoaplysina* buildups, all of which are within the range of the 7128/6–1 data (Fig. 18C). Lønøy (1988) reported the isotope range of late calcite spar to be −11 to −12‰ PDB δ^{18}O and −2.7 to 1.5‰ PDB δ^{13}C, which is similar to the range of the coarse calcite in one of the samples from unit L-2 of 7128/6–1 (Fig. 14A).

The IKU Cores

The third data set is from the ''IKU cores,'' a series of shallow stratigraphic test cores penetrating the Upper Carboniferous–Permian Finnmark carbonate platform succession near its southern erosional truncation against the Norwegian mainland, 30 to 100 km south to southeast of well 7128/6–1 (Bugge et al. 1995; Ehrenberg et al. 2000a). A summary of these data was recently published in Stemmerik et al. (1999). The IKU calcite data (Fig. 18B) show a pattern strikingly different from the 7128/6–1 and 7128/4–1 data in that only a few of the IKU ''blocky'' spar analyses have δ^{18}O more negative than −9‰ PDB, and the IKU δ^{13}C extend to highly negative values. The generally less negative δ^{18}O of the IKU calcites may indicate cementation at lower temperatures than in the exploration wells, consistent with the shallower present burial depths of the IKU cores (< 165 m) compared with the 7128/6–1 and 7128/4–1 cores (1834–2132 m). The four IKU analyses with highly negative δ^{18}O are all from a single sample location (126.7 m in well 7030/03-U-01; at the top of a thin buildup bed), so the general significance of these data is uncertain. The more negative δ^{13}C range of the IKU calcites could reflect involvement of migrated hydrocarbons during cementation. This is supported by the observation that three of the data points with highly negative δ^{13}C are from the interval 19–49 m in core 7029/03-U-02 (Fig. 18B), where vug fillings of coarse calcite plus native sulfur are viewed as the possible product of sulfate

reduction involving a former hydrocarbon column (Ehrenberg et al. 2000a). The IKU dolomite data (Fig. 18C) have a range similar to the exploration-well dataset, except that they do not extend to as negative $\delta^{18}O$ values. This difference probably reflects the absence in the IKU cores of saddle dolomite, which is interpreted as being the latest (highest-temperature) carbonate cement in the exploration-well cores (Table 2).

CONCLUSIONS

The upper Paleozoic of the Barents Sea is a major carbonate and frontier hydrocarbon province, wherein relatively little information was previously available regarding diagenesis and cement geochemistry. This paper gives a detailed look at one area with exceptional core coverage and good development of reservoir quality and reports a number of fundamental relationships that may have wider significance for understanding cement geochemical trends in other carbonate provinces as well.

A strong relationship exists between siliciclastic (clay) content of the local stratigraphic environment and both low carbonate carbon isotope values and enrichment of late cements in Fe and Mn. Thus proximity of shaly beds is an important influence on some aspects of cement geochemistry. The present results also illustrate that cyclic, shallow-water Upper Carboniferous–Lower Permian carbonates are not always characterized by the development of low-$\delta^{13}C$ excursions at cycle tops inferred to represent subaerial exposure surfaces.

The diagenetic history of this thick and heterogeneous photozoan-dominated carbonate succession appears to be relatively simple. Marine cementation in this inner-platform setting was insignificant. The eogenetic stage of aragonite–Mg-calcite dissolution–stabilization, shallow meteoric calcite cementation, and localized hypersalinity-driven early dolomitization produced characteristic fine crystal fabrics lining bioclasts and replacing mud matrix. Later mesogenetic diagenesis appears to have consisted of gradual porosity occlusion by coarser cement overgrowths, possibly supplied by dissolution along stylolites in the immediate stratigraphic environment, with no signs of significant late porosity enhancement. A sharp petrographic discontinuity separates late dolomite and calcite cements from a latest stage of saddle dolomite and anhydrite, although fluid-inclusion data show that the saddle dolomite formed from waters having temperature and salinity not notably different from the preceding coarse calcite and dolomite.

Fluid-inclusion data show that original marine to mixed-meteoric pore waters were replaced throughout the upper Paleozoic section by extremely high-salinity waters before mesogenetic cementation began, possibly reflecting a series of brine-reflux episodes related to successive major lowstands of relative sea level. Thus, diagenesis of the Finnmark Platform was very different from the many well-documented cases where shallow-water platforms experienced massive calcite cementation in response to regional systems of meteoric water flux (Meyers 1978; Grover and Read 1983; de Wet 1987; Dorobek 1987; Hendry 1993). It is also to be noted that free hydrocarbons were absent during late cement growth.

ACKNOWLEDGMENTS

REFERENCES

ALLAN, J.R., AND MATTHEWS, R.K., 1982, Isotope signatures associated with early meteoric diagenesis: Sedimentology, v. 29, p. 797–817.

BOLES, J.R., AND FRANKS, S.G., 1979, Clay diagenesis in Wilcox sandstones of southwest Texas: implications of smectite diagenesis on sandstone cementation: Journal of Sedimentary Petrology, v. 49, p. 55–70.

BUDD, D.A., HAMMES, U., AND WARD, W.B., 2000, Cathodoluminescence in calcite cements: new insights on Pb and Zn sensitizing, Mn activation, and Fe quenching at low trace-element concentrations: Journal of Sedimentary Research, v. 70, p. 217–226.

BUDD, D.A., AND LAND, L.S., 1990, Geochemical imprint of meteoric diagenesis in Holocene ooid sands, Schooner Cays, Bahamas: correlation of calcite cement geochemistry with extant groundwaters: Journal of Sedimentary Petrology, v. 60, p. 361–378.

BUDD, D.A., SALLER, A.H., AND HARRIS, P.M., EDS., 1995, Unconformities and Porosity in Carbonate Strata: American Association of Petroleum Geologists, Memoir 63, 313 p.

BUGGE, T., MANGERUD, G., ELVEBAKK, G., MØRK, A., NILSSON, I., FANAVOLL, S., AND VIGRAN, J.O., 1995, The Upper Palaeozoic succession on the Finnmark Platform, Barents Sea: Norsk Geologisk Tidsskrift, v. 75, p. 3–30.

CHOQUETTE, P.W., AND PRAY, L.C., 1970, Geological nomenclature and classification of porosity in sedimentary carbonates: American Association of Petroleum Geologists, Bulletin, v. 54, p. 207–250.

DENG, X., SUN, Y., LEI, X., AND LU, Q., 1996, Illite/smectite diagenesis in the NanXiang, Yitong, and north China Permian–Carboniferous basins: application to petroleum exploration in China: American Association of Petroleum Geologists, Bulletin, v. 80, p. 157–173.

DE WET, C.B., 1987, Deposition and diagenesis in an extensional basin: the Corallian Formation (Jurassic) near Oxford, England, in Marshall, J.D., ed., Diagenesis of Sedimentary Sequences: Geological Society of London, Special Publication 36, p. 339–353.

DICKENS, G.R., O'NEIL, J.R., REA, D.K., AND OWEN, R.M., 1995, Dissociation of oceanic methane hydrate as a cause for the oceanic carbon isotope excursion at the end of the Paleocene: Paleoceanography, v. 10, p. 965–971.

DOROBEK, S.L., 1987, Petrography, geochemistry, and origin of burial diagenetic facies, Siluro–Devonian Helderberg Group (carbonate rocks), central Appalachians: American Association of Petroleum Geologists, Bulletin, v. 71, p. 492–514.

DRAVIS, J.J., AND YUREWICZ, D.A., 1985, Enhanced carbonate petrography using fluorescence microscopy: Journal of Sedimentary Petrology, v. 55, p. 795–804.

DWORKIN, S.I., AND LAND, L.S., 1994, Petrographic and geochemical constraints on the formation and diagenesis of anhydrite cements, Smackover sandstones, Gulf of Mexico: Journal of Sedimentary Research, v. A64, p. 339–348.

EHRENBERG, S.N., NIELSEN, E.B., SVÅNÅ, T.A., AND STEMMERIK, L., 1998a, Depositional evolution of the Finnmark carbonate platform, Barents Sea: results from wells 7128/6–1 and 7128/4–1: Norsk Geologisk Tidsskrift, v. 78, p. 185–224.

EHRENBERG, S.N., NIELSEN, E.B., SVÅNÅ, T.A., AND STEMMERIK, L., 1998b, Diagenesis and reservoir quality of the Finnmark carbonate platform, Barents Sea: results from wells 7128/6–1 and 7128/4–1: Norsk Geologisk Tidsskrift, v. 78, p. 225–251.

EHRENBERG, S.N., PICKARD, N.A.H., SVÅNÅ, T.A., NILSSON, I., AND DAVYDOV, V.I., 2000a, Sequence stratigraphy of the inner Finnmark carbonate platform (Upper Carboniferous–Permian), Barents Sea—correlation between well 7128/6–1 and the shallow IKU cores: Norsk Geologisk Tidsskrift, v. 80, p. 129–161.

EHRENBERG, S.N., AND SVÅNÅ, T.A., 2001, Use of spectral gamma ray signature to interpret stratigraphic surfaces in carbonate strata: an example from the Finnmark carbonate platform (Carboniferous–Permian), Barents Sea: American Association of Petroleum Geologists, Bulletin, v. 85, p. 295–308.

EHRENBERG, S.N., SVÅNÅ, T.A., PATTERSON, B., AND MEARNS, E.W., 2000b, Neodymium isotope profiling of carbonate platform strata: correlation between siliciclastic provenance signature and sequence stratigraphy: Sedimentary Geology, v. 131, p. 87–95.

EMERY, D., 1987, Trace-element source and mobility during limestone burial diagenesis—an example from the Middle Jurassic of eastern England, in Marshall, J.D., ed., Diagenesis of Sedimentary Sequences: Geological Society of London, Special Publication 36, p. 201–217.

FOLK, R.L., AND SIEDLECKA, A., 1974, The ''Schizohaline'' environments: its sedimentary and diagenetic fabrics as exemplified by Late Paleozoic rocks of Bear Island, Svalbard: Sedimentary Geology, v. 11, p. 1–15.

GIVEN, R.K., AND LOHMANN, K.C., 1985, Derivation of the original isotope composition of Permian marine cements: Journal of Sedimentary Petrology, v. 55, p. 430–439.

GOLDSTEIN, R.H., 1991, Stable isotope signatures associated with paleosols, Pennsylvanian Holder Formation, New Mexico: Sedimentology, v. 38, p. 67–77.

GOLDSTEIN, R.H., AND REYNOLDS, T.J., 1994, Systematics of Fluid Inclusions in Diagenetic Minerals: SEPM, Short Course 31, 199 p.

GOLONKA, J., AND FORD, D., 2000, Pangean (Late Carboniferous–Middle Jurassic) paleoenvironment and lithofacies: Palaeogeography, Palaeoclimatology, Palaeoecology, v. 161, p. 1–34.

GROSSMAN, E.L., 1994, The carbon and oxygen isotope record during the evolution of Pangaea: Carboniferous to Triassic, in Klein, G.D., ed., Pangea: Paleoclimate, Tectonics, and Sedimentation during Accretion, Zenith, and Breakup of a Supercontinent: Geological Society of America, Special Paper 288, p. 207–228.

GROVER, G., JR., AND READ, J.F., 1983, Paleoaquifer and deep burial cements defined by regional cathodoluminescence patterns, Middle Ordovician carbonates, Virginia: American Association of Petroleum Geologists, Bulletin, v. 67, p. 1275–1303.

GROVES, J.R., AND BRENCKLE, P.L., 1997, Graphic correlation in frontier petroleum provinces: application to Upper Paleozoic sections in the Tarim Basin, western China: American Association of Petroleum Geologists, Bulletin, v. 81, p. 1259–1266.

HECKEL, P.H., 1994, Evaluation of evidence for glacio–eustatic control over marine Pennsylvanian cyclothems in North America and consideration of possible tectonic effects, in Den-

nison, J.M., and Ettensohn, F.R., eds., Tectonic and Eustatic Controls on Sedimentary Cycles: SEPM, Concepts in Sedimentology and Paleontology, no. 4, p. 65–87.

HENDRY, J.P., AND MARSHALL, J.D., 1991, Disequilibrium trace element partitioning in Jurassic sparry calcite cements: implications for crystal growth mechanisms during diagenesis: Geological Society of London, Journal, v. 148, p. 835–848.

HENDRY, J.P., 1993, Geological controls on regional subsurface carbonate cementation: an isotopic–paleohydrologic investigation of Middle Jurassic limestones in central England, *in* Horbury, A.D., and Robinson, A.D., eds., Diagenesis and Basin Development: American Association of Petroleum Geologists, Studies in Geology 36, p. 231–260.

HUDSON, J.D., 1977, Stable isotopes and limestone lithification: Geological Society of London, Journal, v. 133, p. 637–660.

IMMENHAUSER, A., CREUSEN, A., ESTEBAN, M., AND VONHOF, H.B., 2000, Recognition and interpretation of polygenetic discontinuity surfaces in the middle Cretaceous Shu'aiba, Nahr Umr, and Natih Formations of northern Oman: GeoArabia, v. 5, p. 299–322.

IRWIN, H., CURTIS, C., AND COLEMAN, M., 1977, Isotopic evidence for source of diagenetic carbonates formed during burial of organic-rich sediments: Nature, v. 269, p. 209–213.

JAMES, N.P., 1997, The cool-water carbonate depositional realm, *in* James, N.P., and Clarke, J.A.D., eds., Cool-Water Carbonates: SEPM, Special Publication 56, p. 1–20.

KAUFMANN, B., 1997, Diagenesis of Middle Devonian carbonate mounds of the Mader Basin (eastern Anti–Atlas, Morocco): Journal of Sedimentary Research, v. 67, p. 945–956.

KENNEDY, M.J., CHRISTIE-BLICK, N., AND SOHL, L.E., 2001, Are Proterozoic cap carbonates and isotopic excursions a record of gas hydrate destabilization following Earth's coldest intervals?: Geology, v. 29, p. 443–446.

KLAPPA, C.F., 1978, Biolithogenesis of Microcodium: elicidation: Sedimentology, v. 25, p. 489–522.

LAND, L.S., 1983, The application of stable isotopes to studies of the origin of dolomite and to problems of diagenesis of clastic sediments, *in* Arthur, M.A., ed., Stable Isotopes in Sedimentary Geology: SEPM, Short Course 10, p. 4–1–4–22.

LØNØY, A., 1988, Environmental setting and diagenesis of Lower Permian *Palaeoaplysina* build-ups and associated sediments from Bjørnøya: implications for exploration of the Barents Sea: Journal of Petroleum Geology, v. 11, p. 141–156.

MACHEL, H.G., AND BURTON, E.A., 1991, Factors governing cathodoluminescence in calcite and dolomite, and their implications for studies of carbonate diagenesis, *in* Barker, C.E., and Kopp, O.C., eds., Luminescence Microscopy and Spectroscopy: Qualitative and Quantitative Applications: SEPM, Short Course 25, p. 37–57.

MARTIROSYAN, V., POPOVA, L., AND VEPREVA, M., 1998, The petroleum systems of the Pechora platform foreland, Russia: Petroleum Geoscience, v. 4, p. 339–348.

MCHARGUE, T.R., AND PRICE, R.C., 1982, Dolomite from clay in argillaceous or shale-associated marine carbonates: Journal of Sedimentary Petrology, v. 52, p. 873–886.

MCKENZIE, J.A., 1981, Holocene dolomitization of calcium carbonate sediments from the coastal sabkhas of Abu Dhabi, U.A.E.: a stable isotope study: Journal of Geology, v. 89, p. 185–198.

MEYERS, W.J., 1978, Carbonate cements: their regional distribution and interpretation in Mississippian limestones of southwestern New Mexico: Sedimentology, v. 25, p. 371–400.

MEYERS, W.J., 1989, Trace element and isotope geochemistry of zoned calcite cements, Lake Valley Formation (Mississippian, New Mexico): insights from rock–water interaction modelling: Sedimentary Geology, v. 65, p. 355–370.

MII, H., GROSSMAN, E.L., AND YANCEY, T.E., 1999, Carboniferous isotope stratigraphies of North America: implications for Carboniferous paleogeography and Mississippian glaciation: Geological Society of America, Bulletin, v. 111, p. 960–973.

MOORE, C.H., 1989, Carbonate Diagenesis and Porosity: Amsterdam, Elsevier, 338 p.

NEVOLIN, N.V., AND FEDOROV, D.L., 1995, Paleozoic pre-salt sediments in the Precaspian petroliferous province: Journal of Petroleum Geology, v. 18, p. 453–470.

OAKES, C.S., BODNAR, R.J., AND SIMONSON, J.M., 1990, The system NaCl–CaCl$_2$–H$_2$O: I. The ice liquidus at 1 atm total pressure: Geochimica et Cosmochimica Acta, v. 54 p. 603–611.

O'NEIL, J.R., CLAYTON, R.N., AND MAYEDA, T.K., 1969, Oxygen isotope fractionation in divalent metal carbonates: Journal of Chemistry and Physics, v. 51, p. 5547–5548.

OLDERSHAW, A.E., AND SCOFFIN, T.P., 1967, The source of ferroan and non-ferroan calcite cements in the Halkin and Wenlock Limestones: Geological Journal, v. 5, p. 309–320.

PEARSON, M.J., AND SMALL, J.S., 1988, Illite–smectite diagenesis and palaeotemperatures in the northern North Sea Quaternary to Mesozoic shale sequences: Clay Minerals, v. 23, p. 109–132.

PICKARD, N.A.H., 1996, Evidence for microbial influence on the development of Lower Carboniferous buildups, *in* Strogen, P., Somerville, I.D., and Jones, G.L., eds., Recent Advances in Lower Carboniferous Geology: Geological Society of London, Special Publication 107, p. 65–82.

PICKARD, N.A.H., EILERTSEN, F., HANKEN, N.-M., JOHANSEN, T.A., LØNØY, A., NAKREM, H.A., NILSSON, I., SAMUELSBERG, T.J., AND SOMERVILLE, I.D., 1996, Stratigraphic framework of Upper Carboniferous (Moscovian–Kasimovian) strata in Bünsow Land, central Spitsbergen: palaeogeographic implications: Norsk Geologisk Tidsskrift, v. 76, p. 169–185.

PIERSON, B.J., 1981, The control of cathodoluminescence in dolomite by iron and manganese: Sedimentology, v. 28, p. 601–610.

ROSS, C.A., AND ROSS, J.R.P., 1988, Late Paleozoic transgressive–regressive deposition, *in* Wilgus, C.K., Hastings, B.S., Kendall, C.G.St.C., Posamentier, H.W., Ross, C.A., and Van Wagoner, J.C., eds., Sea-Level Changes: An Integrated Approach: SEPM, Special Publication 42, p. 227–247.

SALLER, A.H., DICKSON, J.A.D., AND MATSUDA, F., 1999, Evolution and distribution of porosity associated with subaerial exposure in Upper Paleozoic platform limestones, west Texas: American Association of Petroleum Geologists, Bulletin v. 83, p. 1835–1854.

SALLER, A.H., AND MOORE, C.H., JR., 1991, Geochemistry of meteoric calcite cements in some Pleistocene limestones: Sedimentology, v. 38, p. 601–621.

SCHOLLE, P.A., 1995, Carbon and sulfur isotope stratigraphy of the Permian and adjacent intervals, *in* Scholle, P.A., and Peryt, T.M., eds., Permian of the Northern Continents: Berlin, Springer-Verlag, p. 133–149.

SCHOLLE, P.A., AND ARTHUR, M.A., 1980, Carbon isotope fluctuations in Cretaceous pelagic limestones: potential stratigraphic and petroleum exploration tool: American Association of Petroleum Geologists, Bulletin, v. 64, p. 67–87.

SCHOLLE, P.A., AND HALLEY, R.B., 1985, Burial diagenesis: out of sight, out of mind!, *in* Schneidermann, N., and Harris, P.M., eds., Carbonate Cements: SEPM, Special Publication 36, p. 309–334.

SCHNEIDERMANN, N., AND HARRIS, P.M., EDS., 1985, Carbonate Cements: SEPM, Special Publication 36, 379 p.

SELLWOOD, B.W., WILKES, M., AND JAMES, B., 1993, Hydrocarbon inclusions in late calcite cements: migration indicators in the Great Oolite Group, Weald basin, S. England: Sedimentary Geology, v. 84, p. 51–55.

SHINN, E.A., 1986, Modern carbonate tidal flats: their diagnostic features: Colorado School of Mines, Quarterly, v. 81, p. 7–35.

SPÖTL, C, AND PITMAN, J.K., 1998, Saddle (baroque) dolomite in carbonates and sandstones: a reappraisal of a burial-diagenetic concept, *in* Morad, S., ed., Carbonate Cementation in Sandstones: Distribution Patterns and Geochemical Evolution: International Association of Sedimentologists, Special Publication 26, p. 437–460.

STEMMERIK, L., ELVEBAKK, G., AND WORSLEY, D., 1999, Upper Palaeozoic carbonate reservoirs on the Norwegian Arctic Shelf: delineation of reservoir models with application to the Loppa High: Petroleum Geoscience, v. 5, p. 173–187.

STEMMERIK, L., AND LARSSEN, G.B., 1993, Diagenesis and porosity evolution of Lower Permian *Palaeoaplysina* build-ups: an example of diagenetic response to high frequency sea level fluctuations in an arid climate, *in* Horbury, A.D., and Robinson, A.D., eds., Diagenesis and Basin Development: American Association of Petroleum Geologists, Studies in Geology 36, p. 199–211.

VEEVERS, J.J., AND POWELL, C.M.C.A., 1987, Late Paleozoic glacial episodes in Gondwanaland reflected in transgressive–regressive depositional sequences in Euramerica: Geological Society of America, Bulletin, v. 98, p. 475–487.

WAGNER, P.D., TASKER, D.R., AND WAHLMAN, G.P., 1995, Reservoir degradation and compartmentalization below subaerial unconformities: limestone examples from west Texas, China, and Oman, *in* Budd, D.A., Saller, A.H., and Harris, P.M., eds., Unconformities in Carbonate Strata—their Recognition and the Significance of Associated Porosity: American Association of Petroleum Geologists, Memoir 63, p. 177–195.

WORONICK, R.E., AND LAND, L.S., 1985, Late burial diagenesis, Lower Cretaceous Pearsall and lower Glen Rose formations, south Texas: *in* Schneidermann, N., and Harris, P.M., eds., Carbonate Cements: SEPM, Special Publication 36, p. 265–275.

YOO, C.N., GREGG, J.M., AND SHELTON, K.L., 2000, Dolomitization and dolomite neomorphism: Trenton and Black River Limestones (Middle Ordovician) northern Indiana, U.S.A.: Journal of Sedimentary Research, v. 70, p. 265–274.